



1 **The export of African mineral dust across the Atlantic** 2 **and its impact over the Amazon Basin**

3 Xurong Wang^{1,2,a,+}, Qiaoqiao Wang^{1,2,+}, Maria Prass³, Christopher Pöhlker³, Daniel
4 Moran-Zuloaga³, Paulo Artaxo⁴, Jianwei Gu⁵, Ning Yang^{1,2}, Xiajie Yang^{1,2},
5 Jiangchuan Tao^{1,2}, Juan Hong^{1,2}, Nan Ma^{1,2}, Yafang Cheng³, Hang Su³, Meinrat O.
6 Andreae^{3,6}

7 ¹ Institute for Environmental and Climate Research, Jinan University, Guangzhou, 511443, China

8 ² Guangdong-Hongkong-Macau Joint Laboratory of Collaborative Innovation for Environmental
9 Quality, Guangzhou, 511443, China

10 ³ Multiphase Chemistry Department, Max Planck Institute for Chemistry, Mainz, 55128, Germany

11 ⁴ Institute of Physics, University of São Paulo, São Paulo, 05508-900, Brazil

12 ⁵ Institute of Environmental Health and Pollution Control, School of Environmental Science and
13 Engineering, Guangdong University of Technology, Guangzhou, 510006, China

14 ⁶ Scripps Institution of Oceanography, University of California, San Diego, CA 92093-0230, USA

15 ^a now at: Atmospheric Chemistry Department, Max Planck Institute for Chemistry, Mainz, 55128,
16 Germany

17 ⁺ These authors contribute equally to this article

18 Correspondence to, Qiaoqiao Wang (qwang@jnu.edu.cn)

19

20 **Abstract**

21 The Amazon Basin is frequently influenced by the trans-Atlantic transport of African
22 dust plumes during its wet season (January – April), which not only interrupts the
23 near-pristine atmospheric condition in that season, but also provides nutrient inputs
24 into the Amazon rainforest associated with dust deposition. The factors controlling the
25 long-range transport (LRT) of African dust towards the Amazon Basin and
26 consequently the overall impact of African dust over the Amazon Basin are not yet
27 well understood. In this study, we use the chemical transport model GEOS-Chem to
28 investigate the impact of the export of African mineral dust upon the Amazon Basin
29 during the period of 2013 – 2017, constrained by multiple datasets obtained from
30 AERONET, MODIS, as well as Cayenne site and the Amazon Tall Tower Observatory
31 (ATTO) site in the Amazon Basin. With optimized particle mass size distribution
32 (PMSD), the model well captures observed AOD regarding both the mean value as
33 well as the decline rate of the logarithm of AOD over the Atlantic Ocean along the
34 transport path (AOaTP), implying the consistence with observed export efficiency of



35 African dust along the trans-Atlantic transport. With an annual emission of $0.73 \pm$
36 0.12 Pg a^{-1} , African dust entering the Amazon Basin has surface concentrations of 5.7
37 $\pm 1.3 \mu\text{g m}^{-3}$ (up to $15 \mu\text{g m}^{-3}$ in the northeast corner) during the wet season,
38 accounting for $47\% \pm 5.0\%$ (up to 70%) of mass concentrations of total aerosols. The
39 frequency of dust events in the Amazon Basin (defined as when surface dust
40 concentrations reach the threshold of $9 \mu\text{g m}^{-3}$ on daily basis) in the wet season is
41 around 18% averaged over the basin, with maxima over 60% at the northeast coast.
42 During the dust events, AOD over most of the Amazon Basin is dominated by dust.
43 Observed dust peaks over the Amazon Basin are generally associated with relatively
44 higher African dust emissions (including Sahara and Sahel) and longer lifetime of dust
45 along the trans-Atlantic transport, namely higher export efficiency of African dust
46 across the Atlantic Ocean. Associated with dust deposition, we further estimate annual
47 inputs of 52 ± 8.7 , 0.97 ± 0.16 and $21 \pm 3.6 \text{ mg m}^{-2} \text{ a}^{-1}$ for iron, phosphorus and
48 magnesium deposited into the Amazon rainforest, respectively, which may well
49 compensate the hydrologic losses of nutrients in the forest ecosystem.

50

51 **1 Introduction**

52 The desert over North Africa, being the world's largest dust source, contributes to
53 over 50% of global dust emission (Kok et al., 2021; Wang et al., 2016). Dust particles
54 are uplifted by strong surface winds, and then typically transported downwards for a
55 long distance, reaching Atlantic, Caribbean, America and Europe (Prospero et al.,
56 1981; Ben-Ami et al., 2012; Yu et al., 2019; Swap et al., 1992; Prospero et al., 2014;
57 Wang et al., 2020). The emission varies on daily to seasonal and even decadal time
58 scales, largely affected by local wind speed, land surface cover, soil moisture, etc
59 (Ridley et al., 2014; Mahowald et al., 2006). Once present in the atmosphere, mineral
60 dust can degrade air quality downwind as well as modify the atmospheric radiative
61 balance via directly scattering and absorbing solar radiation (Ryder et al., 2013b), and
62 altering cloud properties by acting as cloud condensation nuclei or ice nuclei (Chen et
63 al., 1998; Demott et al., 2003; Mahowald and Kiehl, 2003; Dusek et al., 2006).



64 Additionally, mineral dust contains iron, phosphorous and other nutrients, and could
65 affect ocean biogeochemistry and fertilize tropical forest upon downwind deposition
66 (Niedermeier et al., 2014; Rizzolo et al., 2017).

67 There is an increased concern about the impact of African dust exerted over the
68 Amazon basin, which being the world's largest rainforest, represents a valuable but
69 also vulnerable ecosystem, and is sensitive to any disturbance from climate changes
70 associated with human activities in the future (Andreae et al., 2015; Pöhlker et al.,
71 2019). During the wet season (January – April) Amazonian aerosols are generally
72 dominated by local biogenic aerosol, with remarkably low PM₁₀ mass concentrations
73 of a few $\mu\text{g m}^{-3}$ (Andreae et al., 2015; Martin et al., 2010a; Prass et al., 2021). The
74 near-pristine condition, however, is frequently interrupted by the transatlantic
75 transport of African dust toward the Amazon Basin (Andreae et al., 2015; Martin et
76 al., 2010b; Martin et al., 2010a; Talbot et al., 1990). The dusty episodes could
77 drastically increase the aerosol optical depth (AOD, by a factor of 4), mass
78 concentrations of coarse aerosol (with diameter $> 1 \mu\text{m}$) (up to $100 \mu\text{g m}^{-3}$), as well as
79 crustal elements over the Amazon Basin (Ben-Ami et al., 2010; Pöhlker et al., 2019;
80 Moran-Zuloaga et al., 2018; Baars et al., 2011; Formenti et al., 2001). Therefore, there
81 is great interest in understanding factors controlling the export of African dust towards
82 the Amazon Basin and the impact they might have on the environment, ecosystem,
83 and climate.

84 Over the past decades, field measurements combined with satellite observation and
85 forward/back trajectory analysis have been conducted to explore the long-range
86 transport (LRT) of African dust toward the Amazon Basin (e.g. Ben-Ami et al., 2010;
87 Pöhlker et al., 2018; Prospero et al., 2020). The transatlantic transport of African dust
88 plumes is closely related to annual north-south oscillation of the intertropical
89 convergence zone (ITCZ) (Moran-Zuloaga et al., 2018; Ben-Ami et al., 2012),
90 favoring the path towards the Amazon Basin in the late boreal winter and spring
91 (December-April) as the ITCZ moves southward. In addition to the annual oscillation
92 of ITCZ, the export efficiency of African dust towards the Amazon Basin also highly



93 depends on the lifetime of mineral dust, which is largely affected by the
94 meteorological condition (e.g. precipitation). Dust particles are subject to wet removal
95 when they are within or underneath precipitating clouds. For instance, Yu et al. (2020)
96 argued that El Djouf contributes more dust to the Amazon Basin than the Bodélé
97 depression as the transport paths of dust released from El Djouf are less affected by
98 the rainy cloud.

99 Besides meteorological conditions, dust size distribution can also influence its
100 lifetime and consequently the export efficiency of African dust towards the Amazon
101 Basin. Previous studies have observed that volume/mass fractions of coarse mode dust
102 particles, giant particles in particular, tend to be reduced along the transport due to
103 higher gravitational settling velocities (Ryder et al., 2018; Ryder et al., 2013b; Ryder
104 et al., 2013a; Van Der Does et al., 2016). Moreover, the optical properties of mineral
105 dust are also strongly size dependent, especially for those in sub-micron range (Liu et
106 al., 2018; Di Biagio et al., 2019; Ysard et al., 2018). For instance, Ryder et al. (2013a)
107 reported a loss of 60 – 90% of particles > 30 μm in size 12 h after uplift and
108 consequently an increase in the single scattering albedo from 0.92 to 0.95 associated
109 with the change in the size distribution of dust aerosols. Therefore, the size
110 distribution of dust particles is a key factor determining the efficiency of dust
111 transport and consequently the environmental and climate effect of the mineral dust
112 downwind (Mahowald et al., 2011a; Mahowald et al., 2011b).

113 It is worth mention that the LRT events bring not only mineral dust into the Amazon
114 Basin but also biomass burning aerosols from Africa as well as sea spray aerosols
115 (Wang et al., 2016; Holanda et al., 2020; Andreae et al., 1990; Talbot et al., 1990;
116 Ansmann et al., 2009; Baars et al., 2011), making it challenging to have a quantitative
117 assessment of the impact of African dust on the Amazon Basin. So far, a few studies
118 have attempted to quantify the impact of the LRT of African dust over the Amazon
119 Basin, but mainly focus on dust deposition only (e.g. Yu et al., 2015a; Ridley et al.,
120 2012; Yu et al., 2019). Estimates of annual dust deposition and dust deposition rates
121 into the Amazon Basin exhibit a wide range (7.7-50 Tg a^{-1} and 0.8-19 $\text{g m}^{-2} \text{a}^{-1}$,



122 respectively), attributed to the application of different methods and the intrinsic
123 uncertainties associated with each method (Kok et al., 2021; Yu et al., 2015b;
124 Kaufman, 2005; Swap et al., 1992). For example, the results based on Cloud-Aerosol
125 Lidar and Infrared Pathfinder Satellite Observations (CALIPSO) is subject to the
126 uncertainty associated with the Cloud-Aerosol Lidar with Orthogonal Polarization
127 (CALIOP) extinction, vertical profile shape, dust discrimination, diurnal variations of
128 dust transport as well as the below-cloud dust missed by CALIOP (Yu et al., 2015a).
129 While models could be considered as a useful tool to comprehensively assess the
130 transatlantic transport of African dust towards the Amazon Basin and the consequent
131 impact over the Amazon Basin, there exist considerable differences among model
132 results, attributed to the uncertainties associated with the dust parameterization in the
133 model, including emission schemes, dust size distribution, dust deposition, etc (Kim
134 et al., 2014; Huneus et al., 2011; Mahowald et al., 2014). Observational constraints
135 on the modelling results along the transport from source regions to receptor regions
136 are thus necessarily needed to demonstrate the model performance and to accomplish
137 a better evaluation of factors controlling the variability in the LRT of African dust and
138 its overall impact over the Amazon Basin assessment.

139 Here, we present a detailed multiyear simulation of the export of Africa dust across
140 the Atlantic and the impact over the Amazon Basin (around 8.8×10^6 km², see
141 Figure 1 for defined area) during 2013 – 2017 with the GEOS-Chem (chemical
142 transport model). The aims of this study are: (1) to evaluate the model performance
143 regarding the simulation of dust aerosols including the particle mass size distribution
144 (PMSD), optical properties, mass concentrations as well as the trans-Atlantic transport
145 towards the Amazon Basin; (2) to analyze factors controlling the export of African
146 dust towards the Amazon Basin; and (3) to give a comprehensive examination of the
147 impact of African dust over the Amazon Basin, including aerosol concentrations,
148 AOD and nutrient inputs.

149

150 **2. Methodology**



151 **2.1 GEOS-Chem model**

152 In this study we use the GEOS-Chem model version 12.0.0 (www.geos-chem.org) to
153 perform a global aerosol simulation with a horizontal resolution of $2^\circ \times 2.5^\circ$. The
154 GEOS-Chem is driven by assimilated meteorological data GEOS-FP from the NASA
155 Global Modeling and Assimilation Office (GMAO) (Lucchesi, 2013) with a native
156 horizontal resolution of $0.25^\circ \times 0.3125^\circ$, which is then degraded to $2^\circ \times 2.5^\circ$ for the
157 input to GEOS-Chem. We initialize the model with a 1-year spin-up followed by an
158 aerosol simulation from 2013 to 2017.

159 The aerosol simulation is an offline simulation for aerosol tracers including mineral
160 dust in four size bins, sea salt in fine ($\leq 1 \mu\text{m}$ in diameter) and coarse ($> 1 \mu\text{m}$ in
161 diameter) modes, black carbon (BC), organic aerosols (OA) and sulfate-nitrate-
162 ammonium aerosols. Aerosol optical properties used for aerosol optical depth (AOD)
163 calculation are mainly based on Global Aerosol Data Set (Koepke et al., 1997), with
164 modifications in aerosol size distributions (Jaeglé et al., 2011; Drury et al., 2010;
165 Wang et al., 2003a; Wang et al., 2003b), hygroscopic growth factor of organic
166 aerosols (Jimenez et al., 2009), and the refractive index of dust (Sinyuk et al., 2003).
167 AOD in the model is then calculated online at selected wavelengths assuming
168 lognormal size distributions of externally mixed aerosols and accounts for
169 hygroscopic growth (Martin et al., 2003).

170 Wet deposition in GEOS-Chem, based on the scheme of Liu et al. (2001), accounts for
171 scavenging in both convective updrafts and large-scale precipitation. Further updates
172 by Wang et al. (2011) are also applied, accounting for ice/snow scavenging as well as
173 the impaction scavenging in convective updrafts. Dry deposition in the model follows
174 the standard resistance-in-series scheme by Wesely (2007), accounting for turbulent
175 transfer and gravitational settling (Wang et al., 1998; Zhang et al., 2001).

176 **2.2 Observations**

177 The particle volume size distribution (PVSD) and AOD daily data (at wavelength of
178 675 nm) from AERONET level 2.0
179 (aeronet.gsfc.nasa.gov/new_web/download_all_v3_aod.html, last access on Jun. 22,



180 2021(Dubovik et al., 2002)) during the year of 2013 – 2017 is used in the study to
181 evaluate dust emissions and its PMSD over the source regions in Africa. The PVSD
182 data provided by AERONET is a column-integrated aerosol volume size distribution
183 and with a size range of 0.05 – 15.0 μm . For comparison with model results, the
184 PVSD data is converted to PMSD using the same densities as in the model. In
185 addition, to minimize the influence of aerosols other than dust, only data dominated
186 by coarse aerosol (contribution of fine aerosol to total aerosol volume < 3% or
187 simulated dust contribution > 95%) is used for the comparison.

188 The study also uses observed PMSD over central Sahara during Fennec Campaign
189 (africanclimateoxford.net/projects/fennec/, last access: 22 June 2021) for the
190 comparison with AERONET and our model results. Aiming to investigate dust
191 microphysical and optical properties, 42 profiles of size distribution (0.1 – 300 μm in
192 diameter) over both the Sahara and the Atlantic Ocean, were sampled from in-situ
193 aircraft measurements during Fennec campaign. For more detailed description of the
194 aircraft measurements, readers are referred to Ryder et al. (2013a).

195 In addition, level 3 daily AOD (at wavelength of 550 nm) data from the moderate
196 resolution imaging spectroradiometers (MODIS) installed on Terra and Aqua
197 platforms (<https://ladsweb.modaps.eosdis.nasa.gov/archive/allData/61/>, last access: 22
198 June 2021) is applied in the study to evaluate the trans-Atlantic transport of dust
199 plumes from Africa toward Amazon Basin. For comparison, we degraded the original
200 horizontal resolution of MODIS data ($1^\circ \times 1^\circ$) to $2^\circ \times 2.5^\circ$, consistent with the model
201 outputs.

202 Finally, long-term aerosol measurements at the Amazon Tall Tower Observatory
203 (ATTO, 59.0056° W, 2.1459° S, marked in Figure 1), located in central Amazon Basin
204 are used in the study to evaluate the influence of the long-range transport of African
205 dust over the Amazon Basin. The ATTO site was established in 2012 for the long-term
206 monitoring of climatic, biogeochemical, and atmospheric conditions in the Amazon
207 rainforest. Detailed description of the site and the measurements there could be found
208 in Andreae et al. (2015). In this study, we only use the particle number size



209 distribution from a Optical Particle Sizer (OPS, TSI model 3330; size range of 0.3 –
210 10 μm in diameter, divided into 16 size bins) and a Scanning Mobility Particle Sizer
211 (SMPS, TSI model 3080, St. Paul, MU, USA; size range of 10 – 430 nm in diameter,
212 divided into 104 size bins) over the period from 2014 to 2016. The number size
213 distribution is converted to mass concentrations assuming spherical particles with a
214 constant density of 1.5 g cm^{-3} (Pöschl et al., 2010). In addition, daily PM_{10} mass
215 concentrations during wet season (from January to April) in 2014 measured at
216 Cayenne, French Guiana (4.9489° N , 52.3097° W , located in the northeast coast of the
217 Amazon Basin, marked in Figure 1, <https://doi.org/10.17604/vrsh-w974>) are also used
218 in this study to further evaluate the model performance regarding the trans-Atlantic
219 transport of African dust toward the Amazon basin. The measurement at Cayenne site
220 is carried out on a cooperative basis by personnel of ATMO-Guyane, a non-profit
221 organization (<https://www.atmo-guyane.org/qui-sommes-nous/statuts/>). The PM_{10}
222 samples are measured by a Taper Element Oscillating Microbalance (TEOM, model
223 1400 series, ThermoFisher Scientific) and then are returned to Miami for analysis
224 (Prospero et al., 2020). Readers are referred to Prospero et al. (2020) for detailed
225 description of the site and the data.

226

227 **3 Dust emissions and size distribution**

228 **3.1 Dust emissions**

229 The emission of mineral dust is based on the dust entrainment and deposition (DEAD)
230 mobilization scheme of Zender et al. (2003) in the GEOS-Chem model (Duncan
231 Fairlie et al., 2007). Figure 1 shows the spatial distribution of simulated dust
232 emissions and Table 1 lists seasonal and annual dust emissions in northern Africa
233 ($17.5^\circ \text{ W} - 40^\circ \text{ E}$, $10^\circ \text{ N} - 35^\circ \text{ N}$) for the period of 2013 – 2017. Simulated annual
234 dust emission from northern Africa is $0.73 \pm 0.12 \text{ Pg a}^{-1}$, contributing more than 70%
235 of the global dust emission ($0.99 \pm 0.20 \text{ Pg a}^{-1}$). The result is in the range of $0.42 -$
236 2.05 Pg a^{-1} reported by Kim et al. (2014), who evaluated five AeroCom II global
237 models regarding the dust simulation over similar regions.



238 There exists a strong seasonality in the dust emission from northern Africa, peaking in
239 spring and winter (up to 1.2 Pg a^{-1}) and reaching the minimum in fall (around 0.33 Pg
240 a^{-1}) in general. Previous studies have also pointed out that dust emissions over
241 different African regions show distinct variations (Bakker et al., 2019; Shao et al.,
242 2010), attributed to differences in geographical properties (Knippertz et al., 2007),
243 vegetation cover (Mahowald et al., 2006; Kim et al., 2017), and meteorological
244 mechanisms on a local scale (Alizadeh-Choobari et al., 2014; Wang et al., 2017;
245 Roberts and Knippertz, 2012). Consequently, there exists substantial seasonal change
246 in dust source regions. For instance, during boreal winter, the Bodélé Depression in
247 northern Chad is found to be the most active triggered by the Harmattan winds, while
248 the northwestern African dust sources become less active in contrast with the
249 condition in boreal summer (Ben-Ami et al., 2012; Prospero et al., 2014). Therefore,
250 we further analyze the emission variability over five different source regions in
251 northern Africa (Figure 1 and Table S1). On an annual basis, the contribution to total
252 northern African dust emission is the largest from Region A (west Sahara, $36\% \pm$
253 4.0%), followed by Region D (central Sahel including Bodélé, $21\% \pm 4.7\%$), Region
254 B (central Sahara, $13\% \pm 2.6\%$), Region C (east Sahara, $12\% \pm 1.0\%$), and Region E
255 (west Sahel, $6.5\% \pm 0.64\%$). The emission fluxes, however, are the most intensive in
256 Region D, up to $11 \pm 2.1 \text{ g month}^{-1} \text{ m}^{-2}$ and are generally below $5 \text{ g month}^{-1} \text{ m}^{-2}$ over
257 the other regions. Concerning the seasonality, higher dust emission tends to occur in
258 boreal spring and winter, with the largest emission flux of $19 \pm 4.7 \text{ g month}^{-1} \text{ m}^{-2}$ from
259 Region D. As shown in Figure 2 and S1, the emissions peak in boreal spring for
260 Region A, B and C, but in winter for Region D and E. There is also a secondary peak
261 in summer emissions for Region E. Correlation analysis between dust emissions and
262 meteorological variables suggests that the seasonality is mainly driven by high surface
263 wind speeds (with r of 0.79-0.96 and 0.68-0.97 for the 75th and 95th percentiles of
264 wind speeds, respectively). Apparent negative correlation is also found between
265 precipitation (soil moisture, Figure S2) and dust emission in Region D with r of -0.69
266 (-0.67). Similar seasonality is also reported by Cowie et al. (2014), who suggested



267 that the strongest dust season in winter in central Sahel is driven by strong harmattan
268 winds and frequent Low level Jet breakdown, and the second peak in summer in west
269 Sahel could be explained by the summer monsoon combined with the Sahara Heat
270 Low. The study also suggested the dominance of strong wind frequency in the
271 seasonal variation of the emission frequencies.

272 There is a significant decrease in the annual emission from 0.88 Pg a^{-1} in 2013 to 0.56
273 Pg a^{-1} in 2017. Similarly, studies on African dust variability at decadal and longer time
274 scales also reported an obviously decreasing trend in both dust emissions in Africa
275 and dustiness over the east mid-Atlantic in recent decades since the early 1980s
276 (Ridley et al., 2014; Middleton, 2019; Shao et al., 2013). Evan et al. (2016) pointed
277 out three periods of persistent anomalously low dust concentrations in the 1860s,
278 1950s and 2000s. Weather and climate drivers behind this variability include
279 precipitation, surface wind over northern Africa, Atlantic Multidecadal Oscillation
280 (AMO), North Atlantic Oscillation (NAO), the movement of ITCZ, etc. For example,
281 as shown in Figure S2, there is an obviously increasing trend of AMO over the period
282 2000 – 2015, especially from 2010 to 2015 (data available from [http://www.esrl.](http://www.esrl.noaa.gov)
283 [noaa.gov](http://www.esrl.noaa.gov), last access on July 29, 2021 (Enfield et al., 2001)). This positive AMO
284 phase corresponds to higher North Atlantic sea-surface temperature (SST), and could
285 result in enhanced rainfall in the Sahel and consequently less African dust emissions
286 (Middleton, 2019). A recent study by Yuan et al. (2020) projected decreased surface
287 wind speeds over African dust source regions as well as more precipitation in the
288 Sahel region due to positive interhemispheric contrast in Atlantic SST associated with
289 the global warming, leading to less dust emissions and weaker westward transport.

290 While most regions show decline trends of dust emissions, the emission in Region D
291 shows a slight increase. The variation is mainly associated with surface wind speeds
292 (Figure S3). For instance, the 75th and 95th percentiles of wind speeds decrease by
293 7.0% and 9.1% in Region B but slightly increases by 2.0% and 1.4% in Region D
294 from 2013 to 2017. The r values are in the range of 0.90 – 0.99 between annual dust
295 emissions and the 95th percentile of wind speeds over all the 5 source regions.



296 Significant negative correlation with r of $-0.52 - -0.73$ between annual dust emissions
297 and soil moisture is also found for those regions except for Region D where r is only -
298 0.08.

299 It is also worth noting that the interannual variation in dust emission is much larger
300 during the wet season (0.96 ± 0.25 , Table 1) than on an annual basis (0.73 ± 0.12).
301 Moreover, while the annual emissions gradually decrease from 2013 to 2017, the
302 emissions during the wet season peak in 2015. The obviously different behavior
303 between the annual emissions and emissions during the wet season suggests that
304 predictions of future impact of African dust emissions over the Amazon Basin in
305 response to climate change should focus on the wet season rather than the annual
306 average, as the former is more related to the export of African dust towards the
307 Amazon Basin.

308

309 **3.2 Dust size distribution and its impact on the export efficiency towards the** 310 **Amazon Basin**

311 Freshly emitted dust particles are divided into four size bins in GEOS-Chem: $0.1 -$
312 $1.0 \mu\text{m}$, $1.0 - 1.8 \mu\text{m}$, $1.8 - 3.0 \mu\text{m}$, and $3.0 - 6.0 \mu\text{m}$ in radius. The first size bin is
313 further divided into four sub-bins ($0.1 - 0.18 \mu\text{m}$, $0.18 - 0.3 \mu\text{m}$, $0.3 - 0.6 \mu\text{m}$, and
314 $0.6 - 1.0 \mu\text{m}$ in radius) for the calculation of optical properties. While total dust
315 emissions are not affected, optical properties, atmospheric lifetime and downwind
316 concentrations of dust particles are sensitive to different PMSD schemes.

317 Table 2 shows 3 different PMSD schemes tested in this study: V12, V12_C and
318 V12_F. Scheme V12, which is derived based on scale-invariant fragmentation theory
319 (Kok, 2011) with modification in tunable parameters (Zhang et al., 2013), is a default
320 set in GEOS-Chem. However, this scheme has been only evaluated for US/Asian dust,
321 not for Africa. On the other hand, V12_C was used in older versions of GEOS-Chem
322 and constrained from aircraft measurements during the Saharan Dust Experiment
323 (Ridley et al., 2012; Highwood et al., 2003). In addition, we derived V12_F based on
324 the measurements during the Fennec aircraft observations also focusing on Saharan



325 dust. Among all the three PMSD, V12_C has the largest mass fraction in the first bin
326 (relatively small particles) and the lowest fraction in the last bin (large ones). In
327 contrast, V12_F has the most dust distributed in the last bin (~ 70%) and only a little
328 (around 5%) in the first bin (0.1 – 1.0 μm).

329 Simulated mass extinction efficiency (MEE, also shown in Table 2) at wavelength of
330 550 nm for dust particles in the first sub-bin (0.1 – 0.18 μm) is 3.13 $\text{m}^2 \text{g}^{-1}$, and
331 decreases to 0.16 $\text{m}^2 \text{g}^{-1}$ for those in the last bin (3.0 – 6.0 μm). The lifetime of dust
332 aerosols against deposition are 5.1, 2.2, 1.7 and 0.86 d in the four bins (from small to
333 large size), respectively. Therefore, as mentioned before, although with the same
334 emission, dust AOD and concentrations could vary greatly with PMSD. Here we
335 evaluate all the three PMSD schemes through the comparison with observed mass size
336 distribution of column-integrated aerosol over Africa, AOD over both Africa and the
337 Atlantic Ocean, as well as dust concentrations in the Amazon Basin.

338 Figure 3 shows the mass fractions of column-integrated aerosols retrieved from
339 AERONET sites compared with model results based on different PMSD schemes. The
340 location of the selected AERONET sites with valid data are marked in Figure 1 as
341 purple symbols (including asterisks and circles). The mean mass fractions for each bin
342 from AERONET data are 17%, 27%, 38%, 17%, respectively. The comparison
343 indicates the model results based on V12_C agrees better with the observations. In
344 other words, the model results with other PMSD schemes (V12_F in particular)
345 greatly underestimate the mass fractions in the first bin and overestimate the mass
346 fractions in the last bin. During the Fennec campaign, the aircraft sampled two strong
347 Saharan dust outbreaks with AOD up to 1.1, which may be associated with strong
348 winds favoring the uplift of large particles.

349 Figure 4 shows the times series of daily AOD at wavelength of 675 nm during the
350 year of 2013 – 2017 from both AERONET and model results. The locations of the
351 selected AERONET sites with valid data are shown in Figure 1 as purple circles.
352 Although different PSD schemes have little influence on the correlation between
353 AERONET and model results with most r around 0.6 – 0.7, the normalized mean bias



354 (NMB) has been significantly improved in V12_C, with a range of -12% – 11% (vs. -
355 33% – -11% and -42% – -19% for V12 and V12_F, respectively). The severe
356 underestimation in AOD from V12 and V12_F could be attributed to their relatively
357 higher dust fractions distributed in larger size bins with lower MEE.

358 In addition, we also compare the spatial distributions of simulated AOD over the
359 Atlantic Ocean with MODIS AOD (at 550 nm) averaged over 2013 – 2017 in Figure
360 5a-d. There is a clear decreasing trend in MODIS AOD along the trans-Atlantic
361 transport from Africa towards South America. Although all simulations show similar
362 spatial distributions with declining trends of AOD along the transport, the results from
363 V12_C are the most consistent with MODIS data with the highest r of 0.89 and the
364 smallest NMB of 6.5% among the three schemes (vs. r of 0.85 and 0.81 and NMB of -
365 13% and -19% for V12 and V12_F, respectively).

366 Assuming first-order removal of aerosol along the transport, we derived linear trend
367 lines based on the gradient of the logarithm of AOD against the distance over the
368 Atlantic Ocean along the transport path (AOaTP, 20° – 50° W and 5° S – 25° N,
369 Figure 5e). MODIS AOD decrease from 0.29 ± 0.023 near the coast of Africa to 0.17
370 ± 0.010 at the coast of South America, with a decline rate of 0.019 ± 0.0025 degree⁻¹.
371 A similar decline rate is found for simulated AOD based on V12_C, decreasing from
372 0.28 ± 0.022 to 0.16 ± 0.013 (0.019 ± 0.0029 degree⁻¹). In contrast, simulations with
373 V12 and V12_F exhibit much lower AOD together with relatively steeper slopes of
374 0.021 ± 0.0040 and 0.021 ± 0.0041 , respectively. To specify the impact of different
375 PMSD on the export efficiency of dust aerosols towards the Amazon Basin, Figure 5f
376 also shows simulated dust AOD (DOD) along the transect from 20° to 50° W. The
377 DOD from V12_C decreases from 0.15 ± 0.018 to 0.049 ± 0.088 along the transport,
378 with a decreasing rate of 0.016 ± 0.0014 degree⁻¹. In contrast, DOD decreases from
379 0.097 ± 0.012 to 0.028 ± 0.085 with a slope of 0.018 ± 0.0016 for V12 and decreases
380 from 0.080 ± 0.090 to 0.025 ± 0.084 with a slope of 0.017 ± 0.0014 for V12_F.

381 Lying in the trade wind belt, Cayenne has been taken as the gate of African dust.
382 Hence, the comparison between simulated and observed dust concentrations could



383 evaluate model performance in reproducing the arrival of African dust to the Amazon
384 Basin. As shown in Figure 6a, the simulation from V12_C shows excellent agreement
385 between simulated dust and observed PM₁₀ concentration during wet season, with r
386 around 0.85 and NMB of -39%. The correlation from the other two simulations is
387 similar ($r = 0.86$), but the corresponding NMB is much larger (-57% for V12 and -
388 80% for V12_F). Prospero et al. (2020) did similar analysis at the Cayenne site but
389 concerning the data all year round. Based on the regression line between observed
390 concentrations of PM₁₀ and dust, they obtained a regional background value of PM₁₀
391 ranging from 17 to 22 $\mu\text{g m}^{-3}$, largely attributed to sea salt aerosol, and suggested
392 PM₁₀ values above this range as a proxy for advected dust. Consistent with their
393 results, the regression line between observed PM₁₀ and simulated dust in this study
394 shows a background value of PM₁₀ around 23 $\mu\text{g m}^{-3}$. The slope of the regression line
395 from V12_C is 1.0, also consistent with the value of 0.9 in the study of Prospero et al.
396 (2020), demonstrating the well performance of the model with V12_C in simulating
397 the trans-Atlantic transport of African dust towards the Amazon Basin. In contrast, the
398 regression lines from V12 and V12_F are much steeper, with the slope of 1.4 and 2.1,
399 respectively.

400 We also compare simulated dust concentrations with observed coarse particles at
401 ATTO site in central Amazon in wet season during 2014 – 2016 in Figure 6b. The
402 correlation between observed and simulated data are similar for different PMSD
403 schemes with r of 0.63 – 0.65. But the bias of V12_C is negligible (NMB = -0.27%)
404 while both V12 and V12_F tend to underestimate the coarse aerosol concentrations
405 with NMB of -36% and -55%, respectively. This again implies relatively higher
406 export efficiency of African dust aerosols towards the Amazon Basin with V12_C
407 associated with their relatively higher dust fractions distributed in smaller size bins.
408 Overall, compared with V12 and V12_F schemes, model results based on V12_C are
409 more consistent with the multiple observed data sets, including column-integrated
410 particle size distribution, AOD and surface coarse aerosol concentrations obtained
411 either over sources or downwind of the sources. Therefore, we use the model results



412 from V12_C (hereinafter referred to as model results unless noted otherwise) to
413 investigate the transatlantic transport of dust from Africa and its impact over the
414 Amazon Basin in the following sections.

415

416 **4. Transatlantic transport of African dust**

417 Associated with the annual oscillation of ITCZ, the dust column burden shows a steep
418 east-west gradient across the ocean with two major paths for different seasons (Figure
419 S4): one moves slightly southwest toward South America in boreal winter and spring,
420 and the other moves west towards the Caribbean in boreal summer and fall.

421 Therefore, although higher dust load over the coastal region of North Africa is found
422 in summer ($> 500 \text{ mg m}^{-2}$), dust reaching the Amazon Basin is less than 10 mg m^{-2} . In
423 contrast, dust load over the Amazon Basin could reach up to 50 mg m^{-2} in spring and
424 winter.

425 In addition to the transport path, the changes in dust column burden along the
426 transport towards the Amazon Basin is also sensitive to its removal rate, namely the
427 lifetime against deposition over the Atlantic. Assuming first-order removal of dust
428 aerosols, we further derived seasonal e-folding lifetime (hereinafter referred to as
429 lifetime) of simulated dust during 2013 – 2017, based on the logarithm of the dust
430 column burden against travel time over the AOaTP (Figure 7). Estimated dust lifetime
431 is the shortest ($1.4 \pm 0.098 \text{ d}$) in winter, followed by fall and spring ($1.9 \pm 0.33 \text{ d}$ and
432 $2.3 \pm 0.31 \text{ d}$, respectively), while the lifetime in summer is the longest ($4.2 \pm 0.68 \text{ d}$).
433 The interannual variability of the lifetime is small in winter with relative standard
434 deviation (RSD) of 7.0%, but relatively large in fall with RSD of 17%.

435 The short lifetime in winter is generally associated with high deposition (with $0.18 \pm$
436 0.034 Pg a^{-1} accounting 20% of the emission of Northern Africa, Table S2). As shown
437 in Figure 8, the spatial distribution of dust deposition is similar to that of dust burden,
438 again illustrating the main transport paths. The largest dust deposition flux ($> 1000 \text{ ng}$
439 $\text{m}^{-2} \text{ s}^{-1}$) is found over the source regions in northern Africa, especially in spring and
440 winter, and is mainly due to dry deposition (accounting for more than 80%). As a



441 result, 48% – 64% of total emission in northern Africa is deposited within the source
442 region. The deposition flux over the AOaTP, also shows strong seasonality, with a
443 maximum of $\sim 530 \text{ ng m}^{-2} \text{ s}^{-1}$ in winter and a minimum of $\sim 180 \text{ ng m}^{-2} \text{ s}^{-1}$ in fall, and
444 is mainly driven by wet deposition (accounting for 76% on average). Again, although
445 the emissions are similar in spring and winter, the deposition flux is much larger in
446 winter, consistent with the relatively shorter lifetime in winter discussed above. On
447 the other hand, the highest dust burden ($144 \pm 58 \text{ mg m}^{-2}$) over the AOaTP is found in
448 summer mainly associated with its longer lifetime, followed by 127 ± 24 , 98 ± 35 , and
449 $57 \pm 20 \text{ mg m}^{-2}$ in winter, spring and fall, respectively. The deposition over the
450 AOaTP only accounts for 7.7% of total emission in northern Africa in Spring, in
451 contrast to 20% in in winter.

452 **5. The influence of African dust over the Amazon Basin**

453 **5.1 Surface aerosol concentrations and AOD**

454 Figure 9 shows the time series of observed and simulated aerosol mass concentrations
455 at ATTO in January – June for the period of 2014 – 2016. Observed mean
456 concentration in wet season is $9.3 \pm 7.6 \mu\text{g m}^{-3}$, of which 83% is from coarse aerosol
457 ($7.7 \mu\text{g m}^{-3}$), while simulated concentration is $11 \pm 6.7 \mu\text{g m}^{-3}$, with dust contribution
458 of 65% ($7.2 \mu\text{g m}^{-3}$). The slight model bias could be to some extent explained by the
459 difference in background concentrations (1.9 and $5.1 \mu\text{g m}^{-3}$ for the observation and
460 model data, respectively). During the wet season, observed coarse aerosol
461 concentrations frequently exceed $9 \mu\text{g m}^{-3}$, and could be up to $50 \mu\text{g m}^{-3}$. Most of
462 observed peaks are found in February – March of 2014 and 2016, and in February –
463 April of 2015. The high correlation (r of 0.52 – 0.71) between observed coarse
464 aerosols and simulated dust concentrations suggests that observed strong variation in
465 coarse aerosols is mainly driven by the influence of dust.

466 The dust peaks are generally associated with large dust emission and/or efficient
467 trans-Atlantic transport (e.g. relatively longer lifetime). For example, the relatively
468 higher dust concentrations in the wet season of 2015 (except for February) are
469 generally associated with higher emissions (1.2 – 1.5 Pg a^{-1}) compared with the year



470 of 2014 and 2016 ($0.68 - 1.0 \text{ Pg a}^{-1}$, see Table S3). On the other hand, although
471 emissions in February 2016 (0.95 Pg a^{-1}) is slightly lower than those in February 2014
472 (1.2 Pg a^{-1}), the relatively longer lifetime (1.7 d vs. 1.5 d) may help explain the high
473 dust concentrations during that period. It should be noted that the lifetime estimated
474 here represents the export efficiency averaged over a relatively large domain and
475 long-time scale (e.g. one month). Besides, the influence of African dust on the ATTO
476 site is also subject to the variations of transport paths and precipitation fields.
477 Over the whole Amazon Basin, simulated average surface dust concentrations in the
478 wet season of 2013 – 2017 are $5.7 \pm 1.3 \mu\text{g m}^{-3}$, with maxima over $15 \mu\text{g m}^{-3}$ in the
479 northeast corner of rainforest and a decreasing trend towards southwestern direction
480 (Figure 10). The dust contribution to surface aerosol concentrations is $47\% \pm 5.0\%$
481 (up to 70% in the north corner). The location with the largest dust contributions
482 slightly shifted inland compared to the spatial distribution of dust concentration. This
483 could be explained by higher influence of sea salt aerosols along the coast. The ATTO
484 site has dust concentrations around $8.1 \pm 1.8 \mu\text{g m}^{-3}$ (accounting for $63\% \pm 7.9\%$ of
485 total aerosol concentrations on average) in wet season, and thus could be
486 representative of the whole Amazon Basin. Based on single-particle analysis using a
487 quantitative energy-dispersive electron probe X-ray microanalysis, Wu et al. (2019)
488 found that aged mineral dust and sea salts account for 37 %–70 % of the super-micron
489 aerosol at ATTO site during the wet season, consistent with our result. The
490 contribution of DOD to AOD at 675 nm over most areas of the Amazon Basin (Figure
491 11) is in the range of 10 – 50% ($26\% \pm 4.7\%$ on average) during the wet season of
492 2013 – 2017, with maxima in the northern Amazon Basin. The dust contribution to
493 total AOD is relatively smaller than that to surface aerosol concentrations, mainly
494 because of the relatively lower MEE of dust aerosols compared to other aerosols.

495 **5.2 Frequency of dust events**

496 Figure 10c also shows the frequency of dust events when surface dust concentrations
497 reach the threshold of $9 \mu\text{g m}^{-3}$ on daily basis as defined in Moran-Zuloaga et al.
498 (2018) over the Amazon Basin in the wet season of 2013 – 2017. Dust frequency



499 averaged over the whole region is around $18\% \pm 4.6\%$ and decreases from 50 – 60%
500 at the northeast coast to $< 1\%$ in southern inland. The frequency of dust events at
501 ATTO site is around 32%, close to the median of the range. The interannual variation
502 of the frequency, however, has an opposite trend, with RSD gradually increasing from
503 10% at the northeast coast to over 100% in southern inland (36% at ATTO). During
504 dust events, the dust mass concentration of ATTO reaches $16 \pm 2.9 \mu\text{g m}^{-3}$ (three
505 times as high as that over the whole wet season), accounting for around $77\% \pm 5.8\%$
506 of total aerosol. Similarly, under the influence of the long-range transport of Saharan
507 dust plumes, Moran-Zuloaga et al. (2018) observed mass concentrations $14 \pm 12 \mu\text{g}$
508 m^{-3} for coarse aerosol at the same site, accounting for 93% of total observed aerosol.
509 There also exists large difference in DOD between the whole wet season and dust
510 events: 0.019 ± 0.0047 vs. 0.038 ± 0.0074 (at wavelength of 675 nm) averaged over
511 the Amazon Basin. A maximum of 0.31 on a daily basis is found on 1 Mar 2016 at the
512 northeast corner (55° W , 4° N) of the Amazon Basin during the study period. During
513 dust events, dust aerosols dominate AOD (50% – 60%) over most regions of the
514 Amazon Basin. At ATTO site, DOD is 0.029 ± 0.0076 and 0.054 ± 0.0074 , accounting
515 for 41% and 57% of AOD over the whole wet season and dust events, respectively.
516 The largest dust contribution (up to 84%) with DOD of 0.15 at ATTO site is found on
517 24 Jan 2015. Consistent with our results, previous studies by Baars et al. (2011) and
518 Baars et al. (2012) reported DOD (532 nm) of up to 0.18 and AOD of ~ 0.14 when
519 affected by strong influence of Saharan dust at a similar Amazon site ($60^\circ 2.3' \text{ W}$, 2°
520 $35.9' \text{ S}$).

521

522 **5.3 Dust deposition and related nutrient input**

523 The spatial distribution of dust deposition over the Amazon Basin is also shown in
524 Figure 8. The mean dust deposition flux in wet season is $2.0 \pm 0.35 \text{ g m}^{-2} \text{ a}^{-1}$, much
525 higher than in dry seasons (August to November, $0.35 \pm 0.16 \text{ g m}^{-2} \text{ a}^{-1}$). The maximum
526 ($2.6 \text{ g m}^{-2} \text{ a}^{-1}$) is found in the year 2015 due to relatively large dust emission and
527 efficient trans-Atlantic transport. With emission of $0.96 \pm 0.25 \text{ Pg a}^{-1}$ in wet season



528 $(0.73 \pm 0.12 \text{ Pg a}^{-1})$ on annual average), only 1.9% (1.4%) of African dust is deposited
529 into the Amazon Basin (dominated by wet deposition) while relatively large part is
530 deposited over the AOaTP (13% in the wet season and 14% on annual average) and
531 northern Africa (49% in the wet season).

532 Assuming mass fractions of 4.4%, 0.082%, and 1.8% for iron, phosphorus, and
533 magnesium respectively in the African dust (Bristow et al., 2010; Chiemeka et al.,
534 2007), we derive deposition fluxes of 88 ± 15 , $1.6 \pm 0.29 \text{ mg m}^{-2} \text{ a}^{-1}$ and $36 \pm 6.3 \text{ mg}$
535 $\text{m}^{-2} \text{ a}^{-1}$ for iron, phosphorus and magnesium respectively into the Amazon rainforest
536 during the wet season and 52 ± 8.7 , 0.97 ± 0.16 and $21 \pm 3.6 \text{ mg m}^{-2} \text{ a}^{-1}$ on annual
537 average (Figure 12). It should be noted that there exists large spatial variation of
538 nutrient input into the Amazon Basin associated with the patterns of dust burden and
539 dust deposition flux. The deposition flux decreases from over $70 \text{ mg m}^{-2} \text{ a}^{-1}$ at
540 northeast coast to less than $7 \text{ mg m}^{-2} \text{ a}^{-1}$ in inland for magnesium and decreases
541 from $> 9 \text{ mg m}^{-2} \text{ a}^{-1}$ at northeast coast to less than $1 \text{ mg m}^{-2} \text{ a}^{-1}$ in southwestern Basin
542 for phosphorus during the wet season. Similarly, the deposition flux of iron during the
543 wet season decreases from over $500 \text{ mg m}^{-2} \text{ a}^{-1}$ at northeast coast to less than 15 mg
544 $\text{m}^{-2} \text{ a}^{-1}$ in the southwest and is above $50 \text{ mg m}^{-2} \text{ a}^{-1}$ in most of the Amazon Basin. It
545 seems that the nutrient input from Africa dust may play a significant role in the
546 northeastern part of the Amazon Basin, not in the southwest.

547 Table 3 summarized the estimates of dust and associated phosphorus deposition into
548 the Amazon Basin from previous studies. The estimated fluxes of dust and associated
549 phosphorus deposition are in the range of $0.81 - 19 \text{ g m}^{-2} \text{ a}^{-1}$ and $0.48 - 16 \text{ mg m}^{-2} \text{ a}^{-1}$.
550 The large range is mainly driven by the high values ($19 \text{ g m}^{-2} \text{ a}^{-1}$ and $16 \text{ mg m}^{-2} \text{ a}^{-1}$ for
551 dust and associated phosphorus, respectively) from the study of Swap et al. (1992).
552 Based on observations during storm events and dust climatology, the study estimated
553 dust importation into the northeastern basin, which is most subject to the intrusion of
554 African dust. Besides the discrepancy in defined regions, the wide range could also be
555 partly explained by the application of different methods and associated intrinsic
556 uncertainties as mentioned in the Introduction. For instance, the estimates from Swap



557 et al. (1992) are mainly based on 1-month field measurements at three sites located in
558 the northeastern basin. Assumption about air exchange rate across the coast to the
559 basin, duration of dust storms as well as dust concentrations contained in the dust
560 plumes had to be made to extrapolate the dust deposition into the Amazon Basin.
561 Similarly, bias could also arise from insufficient observations available to constrain
562 models or satellite retrievals. Additional uncertainty may also stem from the
563 assumption about the P mass fraction, ranging from 0.07% to 0.108%. Our results are
564 similar to the finding of Prospero et al. (2020), which has also been constrained by the
565 observation at Cayenne.

566 According to Salati and Vose (1984), the total amount of phosphorous and magnesium
567 is 21.6 g m^{-2} and 29.8 g m^{-2} , respectively, in the ecosystem of the Amazon Basin (14.7
568 and 2.3 g m^{-2} respectively in the soil). On the other hand, Vitousek and Sanford
569 (1986) reported a loss of $0.8 - 4 \text{ mg m}^{-2} \text{ a}^{-1}$ for phosphorus and $810 \text{ mg m}^{-2} \text{ a}^{-1}$ for
570 magnesium in Brazilian ecosystem to surface waters. Estimated nutrient input from
571 African dust in our study accounts for 0.011% and 1.6% of total phosphorous and
572 magnesium in the soil over the Amazon Basin during the wet season (0.0066% and
573 0.91% on annual average), and could almost compensate the hydrologic losses of
574 phosphorous in Brazilian forest ecosystem. Similarly, Abouchami et al. (2013)
575 pointed out that most of the Amazonian rainforest is a system with an internal
576 recycling of nutrients. But the extra influx of nutrients from African dust might
577 account for a significant portion of the net outflux, i.e. dissolved discharge of nutrients
578 into rivers. Keep in mind that the estimates of nutrients influx are subject to the
579 uncertainties in the estimates of dust flux as well as the mass fractions of nutrients
580 contained in the dust. In addition, marine aerosols and biomassburning aerosols
581 mixed with the LRT of African dust may also play a role for certain essential nutrients
582 (Prospero et al., 2020; Abouchami et al., 2013).

583

584 **6. Conclusion**

585 In this study, we use the GEOS-Chem model with optimized particle mass size



586 distribution (PMSD) of dust aerosols to investigate the influence of the export of
587 African dust towards the Amazon Basin during 2013 – 2017. The model performance
588 is constrained by multiple datasets obtained from AERONET, MODIS, as well as
589 Cayenne and ATTO sites in the Amazon Basin, including particle size distribution
590 over Africa, aerosol optical depth (AOD) over Africa and the Atlantic Ocean as well
591 as coarse and total aerosols concentrations in the Amazon Basin.
592 Simulated dust emission from northern Africa is $0.73 \pm 0.12 \text{ Pg a}^{-1}$, accounting for
593 more than 70% of global dust emission. There exists a strong seasonality in dust
594 emission with peaks in spring or winter, which varies with source regions and is
595 mainly driven by high surface wind speeds. It is worth noting that no consistent
596 decline is found for dust emission during the wet season, when the export of African
597 dust towards the Amazon Basin is more efficient driven by the southward movement
598 of ITCZ.
599 In addition to the transport path associated with the oscillation of ITCZ, the export
600 efficiency of African dust towards the Amazon basin is sensitive to the removal of
601 dust aerosol along the trans-Atlantic transport, which also depends on assumed PMSD
602 of dust aerosols in the model. The optimized PMSD in this study well captures
603 observed AOD regarding both the mean value as well as the decline rate of the
604 logarithm of AOD over the Atlantic Ocean along the transport path (AOaTP), while
605 the other two PMSD schemes tend to overestimate the decline rate by 11% and
606 underestimate the mean value by up to ~40%. The study further estimates the e-
607 folding lifetime of dust aerosols along the trans-Atlantic transport based on the
608 logarithm of the dust column burden against travel time over the AOaTP. The shortest
609 lifetime (1.4 d) is found for winter associated with high deposition flux, while the
610 highest dust burden over the AOaTP is found in summer mainly associated with its
611 longer lifetime (4.2 d).
612 Simulated surface dust concentration averaged over the whole Amazon Basin is $5.7 \pm$
613 $1.3 \mu\text{g m}^{-3}$ during the wet season of 2013 – 2017, contributing $47\% \pm 5.0\%$ to total
614 surface aerosols. Observed dust peaks at the ATTO site are generally associated with



615 large dust emission and/or efficient trans-Atlantic transport. The frequency of dust
616 events is $18\% \pm 4.6\%$ averaged over the Amazon Basin and up to 50% – 60% at the
617 northeast coast. During the dust events, DOD is around 0.038 and dominate total
618 AOD over most of the Amazon Basin. Associated with the deposition of African dust,
619 the study estimated annual inputs of 52 ± 8.7 , 0.97 ± 0.16 and 21 ± 3.6 $\text{mg m}^{-2} \text{a}^{-1}$ for
620 iron, phosphorus and magnesium into the Amazon rainforest, which may well
621 compensate the hydrologic losses of nutrients in the forest ecosystem.

622

623 Acknowledgements.

624 This work is supported by the National Natural Science Foundation of China (41907182,
625 41877303, 91644218), the National key R&D Program of China (2018YFC0213901), the
626 Fundamental Research Funds for the Central Universities (21621105), the Guangdong
627 Innovative and Entrepreneurial Research Team Program (Research team on atmospheric
628 environmental roles and effects of carbonaceous species: 2016ZT06N263), and Special Fund
629 Project for Science and Technology Innovation Strategy of Guangdong Province
630 (2019B121205004). We acknowledge the support by the Instituto Nacional de Pesquisas da
631 Amazônia (INPA). We would like to thank all people involved in the technical, logistical, and
632 scientific support within the ATTO project.

633

634 *Financial support.* This work is supported by the National Natural Science Foundation of
635 China (41907182, 41877303, 91644218), the National key R&D Program of China
636 (2018YFC0213901), the Fundamental Research Funds for the Central Universities
637 (21621105), the Guangdong Innovative and Entrepreneurial Research Team Program
638 (Research team on atmospheric environmental roles and effects of carbonaceous species:
639 2016ZT06N263), and Special Fund Project for Science and Technology Innovation Strategy
640 of Guangdong Province (2019B121205004). For the operation of the ATTO site, we
641 acknowledge the support by the Max Planck Society (MPG), the German Federal Ministry of
642 Education and Research (BMBF contracts 01LB1001A, 01LK1602B, and 01LK2101B) and
643 the Brazilian Ministério da Ciência, Tecnologia e Inovação (MCTI/FINEP contract



644 01.11.01248.00), the Amazon State University (UEA), FAPEAM, LBA/INPA, FAPESP -
645 Fundação de Amparo à Pesquisa do Estado de São Paulo, grant number 2017/17047-0, and
646 SDS/CEUC/RDS-Uatumã. XW acknowledges the financial support of China Scholarship
647 Council (CSC). MP acknowledges the financial support by the Max Planck Graduate Center
648 with the Johannes-Gutenberg University, Mainz.

649

650 Competing interests.

651 Hang Su and Yafang Cheng are members of the editorial board of Atmospheric Chemistry and
652 Physics.

653

654 Data availability.

655 OPS data used in this study could be found at <https://www.attodata.org/>. Other datasets are
656 available upon request.

657

658 References

- 659 Abouchami, W., Nätthe, K., Kumar, A., Galer, S. J. G., Jochum, K. P., Williams, E., Horbe, A.
660 M. C., Rosa, J. W. C., Balsam, W., Adams, D., Mezger, K., and Andreae, M. O.:
661 Geochemical and isotopic characterization of the Bodélé Depression dust source and
662 implications for transatlantic dust transport to the Amazon Basin, *Earth Planet. Sc. Lett.*,
663 380, 112-123, <https://doi.org/10.1016/j.epsl.2013.08.028>, 2013.
- 664 Alizadeh-Choobari, O., Sturman, A., and Zawar-Reza, P.: A global satellite view of the
665 seasonal distribution of mineral dust and its correlation with atmospheric circulation,
666 *Dynam. Atmos. Oceans*, 68, 20-34, <https://doi.org/10.1016/j.dynatmoce.2014.07.002>,
667 2014.
- 668 Andreae, M. O., Berresheim, H., Bingemer, H., Jacob, D. J., Lewis, B. L., Li, S.-M., and
669 Talbot, R. W.: The atmospheric sulfur cycle over the Amazon Basin: 2. Wet season, *J.*
670 *Geophys. Res.*, 95, 16813-16824, <https://doi.org/10.1029/JD095iD10p16813>, 1990.
- 671 Andreae, M. O., Acevedo, O. C., Araùjo, A., Artaxo, P., Barbosa, C. G. G., Barbosa, H. M. J.,
672 Brito, J., Carbone, S., Chi, X., Cintra, B. B. L., da Silva, N. F., Dias, N. L., Dias-Júnior,
673 C. Q., Ditas, F., Ditz, R., Godoi, A. F. L., Godoi, R. H. M., Heimann, M., Hoffmann, T.,
674 Kesselmeier, J., Könemann, T., Krüger, M. L., Lavric, J. V., Manzi, A. O., Lopes, A. P.,
675 Martins, D. L., Mikhailov, E. F., Moran-Zuloaga, D., Nelson, B. W., Nölscher, A. C.,
676 Santos Nogueira, D., Piedade, M. T. F., Pöhlker, C., Pöschl, U., Quesada, C. A., Rizzo,
677 L. V., Ro, C. U., Ruckteschler, N., Sá, L. D. A., de Oliveira Sá, M., Sales, C. B., dos
678 Santos, R. M. N., Saturno, J., Schöngart, J., Sörgel, M., de Souza, C. M., de Souza, R. A.
679 F., Su, H., Targhetta, N., Tóta, J., Trebs, I., Trumbore, S., van Eijck, A., Walter, D.,
680 Wang, Z., Weber, B., Williams, J., Winderlich, J., Wittmann, F., Wolff, S., and Yáñez-



- 681 Serrano, A. M.: The Amazon Tall Tower Observatory (ATTO): overview of pilot
682 measurements on ecosystem ecology, meteorology, trace gases, and aerosols, *Atmos.*
683 *Chem. Phys.*, 15, 10723-10776, 10.5194/acp-15-10723-2015, 2015.
- 684 Ansmann, A., Baars, H., Tesche, M., Müller, D., Althausen, D., Engelmann, R., Pauliquevis,
685 T., and Artaxo, P.: Dust and smoke transport from Africa to South America: Lidar
686 profiling over Cape Verde and the Amazon rainforest, *Geophys. Res. Lett.*, 36,
687 <https://doi.org/10.1029/2009GL037923>, 2009.
- 688 Baars, H., Ansmann, A., Althausen, D., Engelmann, R., Artaxo, P., Pauliquevis, T., and Souza,
689 R.: Further evidence for significant smoke transport from Africa to Amazonia, *Geophys.*
690 *Res. Lett.*, 38, <https://doi.org/10.1029/2011GL049200>, 2011.
- 691 Baars, H., Ansmann, A., Althausen, D., Engelmann, R., Heese, B., Müller, D., Artaxo, P.,
692 Paixao, M., Pauliquevis, T., and Souza, R.: Aerosol profiling with lidar in the Amazon
693 Basin during the wet and dry season, *J. Geophys. Res.*, 117,
694 <https://doi.org/10.1029/2012JD018338>, 2012.
- 695 Bakker, N. L., Drake, N. A., and Bristow, C. S.: Evaluating the relative importance of
696 northern African mineral dust sources using remote sensing, *Atmos. Chem. Phys.*, 19,
697 10525-10535, 10.5194/acp-19-10525-2019, 2019.
- 698 Barkley, A. E., Prospero, J. M., Mahowald, N., Hamilton, D. S., Pependorf, K. J., Oehlert, A.
699 M., Pourmand, A., Gatineau, A., Panechou-Pulcherie, K., Blackwelder, P., and Gaston,
700 C. J.: African biomass burning is a substantial source of phosphorus deposition to the
701 Amazon, Tropical Atlantic Ocean, and Southern Ocean, *Proceedings of the National*
702 *Academy of Sciences*, 116, 16216-16221, 10.1073/pnas.1906091116, 2019.
- 703 Ben-Ami, Y., Koren, I., Altaratz, O., Kostinski, A., and Lehahn, Y.: Discernible rhythm in the
704 spatio/temporal distributions of transatlantic dust, *Atmos. Chem. Phys.*, 12, 2253-2262,
705 10.5194/acp-12-2253-2012, 2012.
- 706 Ben-Ami, Y., Koren, I., Rudich, Y., Artaxo, P., Martin, S. T., and Andreae, M. O.: Transport of
707 North African dust from the Bodélé depression to the Amazon Basin: a case study,
708 *Atmos. Chem. Phys.*, 10, 7533-7544, 10.5194/acp-10-7533-2010, 2010.
- 709 Bristow, C. S., Hudson-Edwards, K. A., and Chappell, A.: Fertilizing the Amazon and
710 equatorial Atlantic with West African dust, *Geophys. Res. Lett.*, 37,
711 <https://doi.org/10.1029/2010GL043486>, 2010.
- 712 Chen, Y., Kreidenweis, S. M., McInnes, L. M., Rogers, D. C., and DeMott, P. J.: Single
713 particle analyses of ice nucleating aerosols in the upper troposphere and lower
714 stratosphere, *Geophys. Res. Lett.*, 25, 1391-1394, 10.1029/97gl03261, 1998.
- 715 Chiemeka, I. U., Oleka, M. O., and Chineke, T.: Determination of aerosol metal composition
716 and concentration during the 2001/2002 Harmattan season at Uturu, Nigeria, *Global J.*
717 *Pure Appl. Sci.*, 13, 10.4314/gjpas.v13i3.16734, 2007.
- 718 Cowie, S. M., Knippertz, P., and Marsham, J. H.: A climatology of dust emission events from
719 northern Africa using long-term surface observations, *Atmos. Chem. Phys.*, 14, 8579-
720 8597, 10.5194/acp-14-8579-2014, 2014.
- 721 Demott, P. J., Sassen, K., Poellot, M. R., Baumgardner, D., Rogers, D. C., Brooks, S. D.,
722 Prenni, A. J., and Kreidenweis, S. M.: African dust aerosols as atmospheric ice nuclei,
723 *Geophys. Res. Lett.*, 30, <https://doi.org/10.1029/2003GL017410>, 2003.
- 724 Di Biagio, C., Formenti, P., Balkanski, Y., Caponi, L., Cazaunau, M., Pangui, E., Journet, E.,



- 725 Nowak, S., Andreae, M. O., Kandler, K., Saeed, T., Piketh, S., Seibert, D., Williams, E.,
726 and Doussin, J. F.: Complex refractive indices and single-scattering albedo of global dust
727 aerosols in the shortwave spectrum and relationship to size and iron content, *Atmos.*
728 *Chem. Phys.*, 19, 15503-15531, 10.5194/acp-19-15503-2019, 2019.
- 729 Drury, E., Jacob, D. J., Spurr, R. J. D., Wang, J., Shinozuka, Y., Anderson, B. E., Clarke, A.
730 D., Dibb, J., McNaughton, C., and Weber, R.: Synthesis of satellite (MODIS), aircraft
731 (ICARTT), and surface (IMPROVE, EPA-AQS, AERONET) aerosol observations over
732 eastern North America to improve MODIS aerosol retrievals and constrain surface
733 aerosol concentrations and sources, *J. Geophys. Res.*, 115,
734 <https://doi.org/10.1029/2009JD012629>, 2010.
- 735 Dubovik, O., Holben, B., Eck, T. F., Smirnov, A., Kaufman, Y. J., King, M. D., Tanré, D., and
736 Slutsker, I.: Variability of Absorption and Optical Properties of Key Aerosol Types
737 Observed in Worldwide Locations, *J. Atmos. Sci.*, 59, 590-608,
738 [http://doi.org/10.1175/1520-0469\(2002\)059<0590:VOAOP>2.0.CO;2](http://doi.org/10.1175/1520-0469(2002)059<0590:VOAOP>2.0.CO;2), 2002.
- 739 Duncan Fairlie, T., Jacob, D. J., and Park, R. J.: The impact of transpacific transport of
740 mineral dust in the United States, *Atmos. Environ.*, 41, 1251-1266,
741 <https://doi.org/10.1016/j.atmosenv.2006.09.048>, 2007.
- 742 Dusek, U., Frank, G. P., Hildebrandt, L., Curtius, J., Schneider, J., Walter, S., Chand, D.,
743 Drewnick, F., Hings, S., Jung, D., Borrmann, S., and Andreae, M. O.: Size Matters More
744 Than Chemistry for Cloud-Nucleating Ability of Aerosol Particles, *Science*, 312, 1375-
745 1378, doi:10.1126/science.1125261, 2006.
- 746 Enfield, D. B., Mestas-Nuñez, A. M., and Trimble, P. J.: The Atlantic Multidecadal
747 Oscillation and its relation to rainfall and river flows in the continental U.S, *Geophys.*
748 *Res. Lett.*, 28, 2077-2080, <https://doi.org/10.1029/2000GL012745>, 2001.
- 749 Evan, A. T., Flamant, C., Gaetani, M., and Guichard, F.: The past, present and future of
750 African dust, *Nature*, 531, 493-495, 10.1038/nature17149, 2016.
- 751 Formenti, P., Andreae, M. O., Lange, L., Roberts, G., Cafmeyer, J., Rajta, I., Maenhaut, W.,
752 Holben, B. N., Artaxo, P., and Lelieveld, J.: Saharan dust in Brazil and Suriname during
753 the Large-Scale Biosphere-Atmosphere Experiment in Amazonia (LBA) - Cooperative
754 LBA Regional Experiment (CLAIRE) in March 1998, *J. Geophys. Res.*, 106, 14919-
755 14934, 10.1029/2000JD900827, 2001.
- 756 Gläser, G., Wernli, H., Kerkweg, A., and Teubler, F.: The transatlantic dust transport from
757 North Africa to the Americas—Its characteristics and source regions, *Journal of*
758 *Geophysical Research: Atmospheres*, 120, 11,231-211,252,
759 <https://doi.org/10.1002/2015JD023792>, 2015.
- 760 Herbert, R. J., Krom, M. D., Carslaw, K. S., Stockdale, A., Mortimer, R. J. G., Benning, L. G.,
761 Pringle, K., and Browse, J.: The Effect of Atmospheric Acid Processing on the Global
762 Deposition of Bioavailable Phosphorus From Dust, *Global Biogeochemical Cycles*, 32,
763 1367-1385, <https://doi.org/10.1029/2018GB005880>, 2018.
- 764 Highwood, E. J., Haywood, J. M., Silverstone, M. D., Newman, S. M., and Taylor, J. P.:
765 Radiative properties and direct effect of Saharan dust measured by the C-130 aircraft
766 during Saharan Dust Experiment (SHADE): 2. Terrestrial spectrum, *J. Geophys. Res.*,
767 108, <https://doi.org/10.1029/2002JD002552>, 2003.
- 768 Holanda, B. A., Pöhlker, M. L., Walter, D., Saturno, J., Sörgel, M., Ditas, J., Ditas, F., Schulz,



- 769 C., Franco, M. A., Wang, Q., Donth, T., Artaxo, P., Barbosa, H. M. J., Borrmann, S.,
770 Braga, R., Brito, J., Cheng, Y., Dollner, M., Kaiser, J. W., Klimach, T., Knote, C., Krüger,
771 O. O., Fütterer, D., Lavrič, J. V., Ma, N., Machado, L. A. T., Ming, J., Morais, F. G.,
772 Paulsen, H., Sauer, D., Schlager, H., Schneider, J., Su, H., Weinzierl, B., Walser, A.,
773 Wendisch, M., Ziereis, H., Zöger, M., Pöschl, U., Andreae, M. O., and Pöhlker, C.:
774 Influx of African biomass burning aerosol during the Amazonian dry season through
775 layered transatlantic transport of black carbon-rich smoke, *Atmos. Chem. Phys.*, 20,
776 4757-4785, 10.5194/acp-20-4757-2020, 2020.
- 777 Huneus, N., Schulz, M., Balkanski, Y., Griesfeller, J., Prospero, J., Kinne, S., Bauer, S.,
778 Boucher, O., Chin, M., Dentener, F., Diehl, T., Easter, R., Fillmore, D., Ghan, S.,
779 Ginoux, P., Grini, A., Horowitz, L., Koch, D., Krol, M. C., Landing, W., Liu, X.,
780 Mahowald, N., Miller, R., Morcrette, J. J., Myhre, G., Penner, J., Perlwitz, J., Stier, P.,
781 Takemura, T., and Zender, C. S.: Global dust model intercomparison in AeroCom phase
782 I, *Atmos. Chem. Phys.*, 11, 7781-7816, 10.5194/acp-11-7781-2011, 2011.
- 783 Jaeglé, L., Quinn, P. K., Bates, T. S., Alexander, B., and Lin, J. T.: Global distribution of sea
784 salt aerosols: new constraints from in situ and remote sensing observations, *Atmos.*
785 *Chem. Phys.*, 11, 3137-3157, 10.5194/acp-11-3137-2011, 2011.
- 786 Jimenez, J. L., Canagaratna, M. R., Donahue, N. M., Prevot, A. S. H., Zhang, Q., Kroll, J. H.,
787 DeCarlo, P. F., Allan, J. D., Coe, H., Ng, N. L., Aiken, A. C., Docherty, K. S., Ulbrich, I.
788 M., Grieshop, A. P., Robinson, A. L., Duplissy, J., Smith, J. D., Wilson, K. R., Lanz, V.
789 A., Hueglin, C., Sun, Y. L., Tian, J., Laaksonen, A., Raatikainen, T., Rautiainen, J.,
790 Vaattovaara, P., Ehn, M., Kulmala, M., Tomlinson, J. M., Collins, D. R., Cubison, M. J.,
791 Dunlea, J., Huffman, J. A., Onasch, T. B., Alfarra, M. R., Williams, P. I., Bower, K.,
792 Kondo, Y., Schneider, J., Drewnick, F., Borrmann, S., Weimer, S., Demerjian, K.,
793 Salcedo, D., Cottrell, L., Griffin, R., Takami, A., Miyoshi, T., Hatakeyama, S., Shimono,
794 A., Sun, J. Y., Zhang, Y. M., Dzepina, K., Kimmel, J. R., Sueper, D., Jayne, J. T.,
795 Herndon, S. C., Trimborn, A. M., Williams, L. R., Wood, E. C., Middlebrook, A. M.,
796 Kolb, C. E., Baltensperger, U., and Worsnop, D. R.: Evolution of Organic Aerosols in the
797 Atmosphere, *Science*, 326, 5959, 1525-1529, doi:10.1126/science.1180353, 2009.
- 798 Kaufman, Y. J.: Dust transport and deposition observed from the Terra-Moderate Resolution
799 Imaging Spectroradiometer (MODIS) spacecraft over the Atlantic Ocean, *Journal of*
800 *Geophysical Research*, 110, 10.1029/2003jd004436, 2005
- 801 Kim, D., Chin, M., Remer, L. A., Diehl, T., Bian, H., Yu, H., Brown, M. E., and Stockwell, W.
802 R.: Role of surface wind and vegetation cover in multi-decadal variations of dust
803 emission in the Sahara and Sahel, *Atmos. Environ.*, 148, 282-296,
804 <https://doi.org/10.1016/j.atmosenv.2016.10.051>, 2017.
- 805 Kim, D., Chin, M., Yu, H., Diehl, T., Tan, Q., Kahn, R. A., Tsigaridis, K., Bauer, S. E.,
806 Takemura, T., Pozzoli, L., Bellouin, N., Schulz, M., Peyridieu, S., Chédin, A., and Koffi,
807 B.: Sources, sinks, and transatlantic transport of North African dust aerosol: A
808 multimodel analysis and comparison with remote sensing data, *J. Geophys. Res.*, 119,
809 6259-6277, <https://doi.org/10.1002/2013JD021099>, 2014.
- 810 Knippertz, P., Deutscher, C., Kandler, K., Müller, T., Schulz, O., and Schütz, L.: Dust
811 mobilization due to density currents in the Atlas region: Observations from the Saharan
812 Mineral Dust Experiment 2006 field campaign, *J. Geophys. Res.*, 112,



- 813 <https://doi.org/10.1029/2007JD008774>, 2007.
- 814 Koepke, P., Hess, M., Schult, I., and Shettle, E. P.: Global aerosol data set, Max-Planck
815 Institute for Meteorology, 44, 1997.
- 816 Kok, J. F.: A scaling theory for the size distribution of emitted dust aerosols suggests climate
817 models underestimate the size of the global dust cycle, *Proc Natl Acad Sci U S A*, 108,
818 1016-1021, [10.1073/pnas.1014798108](https://doi.org/10.1073/pnas.1014798108), 2011.
- 819 Kok, J. F., Adebisi, A. A., Albani, S., Balkanski, Y., Checa-Garcia, R., Chin, M., Colarco, P.
820 R., Hamilton, D. S., Huang, Y., Ito, A., Klose, M., Li, L., Mahowald, N. M., Miller, R.
821 L., Obiso, V., Pérez Garcia-Pando, C., Rocha-Lima, A., and Wan, J. S.: Contribution of
822 the world's main dust source regions to the global cycle of desert dust, *Atmos. Chem.
823 Phys.*, 21, 8169-8193, [10.5194/acp-21-8169-2021](https://doi.org/10.5194/acp-21-8169-2021), 2021.
- 824 Li, Y., Randerson, J. T., Mahowald, N. M., and Lawrence, P. J.: Deforestation Strengthens
825 Atmospheric Transport of Mineral Dust and Phosphorus from North Africa to the
826 Amazon, *Journal of Climate*, 34, 6087-6096, [10.1175/jcli-d-20-0786.1](https://doi.org/10.1175/jcli-d-20-0786.1), 2021.
- 827 Liu, D., Taylor, J. W., Crosier, J., Marsden, N., Bower, K. N., Lloyd, G., Ryder, C. L., Brooke,
828 J. K., Cotton, R., Marengo, F., Blyth, A., Cui, Z., Estelles, V., Gallagher, M., Coe, H., and
829 Choulaton, T. W.: Aircraft and ground measurements of dust aerosols over the west
830 African coast in summer 2015 during ICE-D and AER-D, *Atmos. Chem. Phys.*, 18,
831 3817-3838, [10.5194/acp-18-3817-2018](https://doi.org/10.5194/acp-18-3817-2018), 2018.
- 832 Liu, H., Jacob, D. J., Bey, I., and Yantosca, R. M.: Constraints from ²¹⁰Pb and ⁷Be on wet
833 deposition and transport in a global three-dimensional chemical tracer model driven by
834 assimilated meteorological fields, *J. Geophys. Res.*, 106, 12109-12128,
835 <https://doi.org/10.1029/2000JD900839>, 2001.
- 836 Lucchesi, R.: File Specification for GEOS-5 FP, GMAO Office Note No.4 (Version 1.0), 63
837 pp., available at: http://gmao.gsfc.nasa.gov/pubs/office_notes, 2013.
- 838 Mahowald, N., Albani, S., Engelstaedter, S., Winckler, G., and Goman, M.: Model insight into
839 glacial–interglacial paleodust records, *Quaternary Sci. Rev.*, 30, 832-854,
840 <https://doi.org/10.1016/j.quascirev.2010.09.007>, 2011a.
- 841 Mahowald, N., Albani, S., Kok, J. F., Engelstaedter, S., Scanza, R., Ward, D. S., and Flanner,
842 M. G.: The size distribution of desert dust aerosols and its impact on the Earth system,
843 *Aeolian Res.*, 15, 53-71, <https://doi.org/10.1016/j.aeolia.2013.09.002>, 2014.
- 844 Mahowald, N. M., Artaxo, P., Baker, A. R., Jickells, T. D., Okin, G. S., Randerson, J. T., and
845 Townsend, A. R.: Impacts of biomass burning emissions and land use change on
846 Amazonian atmospheric phosphorus cycling and deposition, *Global Biogeochemical
847 Cycles*, 19, <https://doi.org/10.1029/2005GB002541>, 2005.
- 848 Mahowald, N., Ward, D. S., Kloster, S., Flanner, M. G., Heald, C. L., Heavens, N. G., Hess, P.
849 G., Lamarque, J.-F., and Chuang, P. Y.: Aerosol Impacts on Climate and
850 Biogeochemistry, *Annu. Rev. Env. Resour.*, 36, 45-74, [10.1146/annurev-environ-042009-
851 094507](https://doi.org/10.1146/annurev-environ-042009-094507), 2011b.
- 852 Mahowald, N. M. and Kiehl, L. M.: Mineral aerosol and cloud interactions, *Geophys. Res.
853 Lett.*, 30, <https://doi.org/10.1029/2002GL016762>, 2003.
- 854 Mahowald, N. M., Muhs, D. R., Levis, S., Rasch, P. J., Yoshioka, M., Zender, C. S., and Luo,
855 C.: Change in atmospheric mineral aerosols in response to climate: Last glacial period,
856 preindustrial, modern, and doubled carbon dioxide climates, *J. Geophys. Res.*, 111,



- 857 <https://doi.org/10.1029/2005JD006653>, 2006.
- 858 Martin, R. V., Jacob, D. J., Yantosca, R. M., Chin, M., and Ginoux, P.: Global and regional
859 decreases in tropospheric oxidants from photochemical effects of aerosols, *J. Geophys.*
860 *Res.*, 108, <https://doi.org/10.1029/2002JD002622>, 2003.
- 861 Martin, S. T., Andreae, M. O., Artaxo, P., Baumgardner, D., Chen, Q., Goldstein, A. H.,
862 Guenther, A., Heald, C. L., Mayol-Bracero, O. L., McMurry, P. H., Pauliquevis, T.,
863 Pöschl, U., Prather, K. A., Roberts, G. C., Saleska, S. R., Silva Dias, M. A., Spracklen,
864 D. V., Swietlicki, E., and Trebs, I.: Sources and properties of Amazonian aerosol
865 particles, *Rev. Geophys.*, 48, <https://doi.org/10.1029/2008RG000280>, 2010a.
- 866 Martin, S. T., Andreae, M. O., Althausen, D., Artaxo, P., Baars, H., Borrmann, S., Chen, Q.,
867 Farmer, D. K., Guenther, A., Gunthe, S. S., Jimenez, J. L., Karl, T., Longo, K., Manzi,
868 A., Müller, T., Pauliquevis, T., Petters, M. D., Prenni, A. J., Pöschl, U., Rizzo, L. V.,
869 Schneider, J., Smith, J. N., Swietlicki, E., Tota, J., Wang, J., Wiedensohler, A., and Zorn,
870 S. R.: An overview of the Amazonian Aerosol Characterization Experiment 2008
871 (AMAZE-08), *Atmos. Chem. Phys.*, 10, 11415-11438, [10.5194/acp-10-11415-2010](https://doi.org/10.5194/acp-10-11415-2010),
872 2010b.
- 873 Middleton, N.: Variability and Trends in Dust Storm Frequency on Decadal Timescales:
874 Climatic Drivers and Human Impacts, *Geosciences*, 9, 261,
875 <http://doi.org/10.3390/geosciences9060261>, 2019.
- 876 Moran-Zuloaga, D., Ditas, F., Walter, D., Saturno, J., Brito, J., Carbone, S., Chi, X., Hrabě de
877 Angelis, I., Baars, H., Godoi, R. H. M., Heese, B., Holanda, B. A., Lavrič, J. V., Martin,
878 S. T., Ming, J., Pöhlker, M. L., Ruckteschler, N., Su, H., Wang, Y., Wang, Q., Wang, Z.,
879 Weber, B., Wolff, S., Artaxo, P., Pöschl, U., Andreae, M. O., and Pöhlker, C.: Long-term
880 study on coarse mode aerosols in the Amazon rain forest with the frequent intrusion of
881 Saharan dust plumes, *Atmos. Chem. Phys.*, 18, 10055-10088, [10.5194/acp-18-10055-](https://doi.org/10.5194/acp-18-10055-2018)
882 2018, 2018.
- 883 Niedermeier, N., Held, A., Müller, T., Heinold, B., Schepanski, K., Tegen, I., Kandler, K.,
884 Ebert, M., Weinbruch, S., Read, K., Lee, J., Fomba, K. W., Müller, K., Herrmann, H.,
885 and Wiedensohler, A.: Mass deposition fluxes of Saharan mineral dust to the tropical
886 northeast Atlantic Ocean: an intercomparison of methods, *Atmos. Chem. Phys.*, 14,
887 2245-2266, [10.5194/acp-14-2245-2014](https://doi.org/10.5194/acp-14-2245-2014), 2014.
- 888 Pöhlker, C., Walter, D., Paulsen, H., Könemann, T., Rodríguez-Caballero, E., Moran-Zuloaga,
889 D., Brito, J., Carbone, S., Degrendele, C., Després, V. R., Ditas, F., Holanda, B. A.,
890 Kaiser, J. W., Lammel, G., Lavrič, J. V., Ming, J., Pickersgill, D., Pöhlker, M. L., Praß,
891 M., Löbs, N., Saturno, J., Sörgel, M., Wang, Q., Weber, B., Wolff, S., Artaxo, P., Pöschl,
892 U., and Andreae, M. O.: Land cover and its transformation in the backward trajectory
893 footprint region of the Amazon Tall Tower Observatory, *Atmos. Chem. Phys.*, 19, 8425-
894 8470, [10.5194/acp-19-8425-2019](https://doi.org/10.5194/acp-19-8425-2019), 2019.
- 895 Pöhlker, M. L., Ditas, F., Saturno, J., Klimach, T., Hrabě de Angelis, I., Araújo, A. C., Brito,
896 J., Carbone, S., Cheng, Y., Chi, X., Ditz, R., Gunthe, S. S., Holanda, B. A., Kandler, K.,
897 Kesselmeier, J., Könemann, T., Krüger, O. O., Lavrič, J. V., Martin, S. T., Mikhailov, E.,
898 Moran-Zuloaga, D., Rizzo, L. V., Rose, D., Su, H., Thalman, R., Walter, D., Wang, J.,
899 Wolff, S., Barbosa, H. M. J., Artaxo, P., Andreae, M. O., Pöschl, U., and Pöhlker, C.:
900 Long-term observations of cloud condensation nuclei over the Amazon rain forest – Part



- 901 2: Variability and characteristics of biomass burning, long-range transport, and pristine
902 rain forest aerosols, *Atmos. Chem. Phys.*, 18, 10289-10331, 10.5194/acp-18-10289-
903 2018, 2018.
- 904 Pöschl, U., Martin, S. T., Sinha, B., Chen, Q., Gunthe, S. S., Huffman, J. A., Borrmann, S.,
905 Farmer, D. K., Garland, R. M., Helas, G., Jimenez, J. L., King, S. M., Manzi, A.,
906 Mikhailov, E., Pauliquevis, T., Petters, M. D., Prenni, A. J., Roldin, P., Rose, D.,
907 Schneider, J., Su, H., Zorn, S. R., Artaxo, P., and Andreae, M. O.: Rainforest Aerosols as
908 Biogenic Nuclei of Clouds and Precipitation in the Amazon, *Science*, 329, 1513-1516,
909 doi:10.1126/science.1191056, 2010.
- 910 Prass, M., Andreae, M. O., de Araujo, A. C., Artaxo, P., Ditas, F., Elbert, W., Förster, J. D.,
911 Franco, M. A., Hrabě de Angelis, I., Kesselmeier, J., Klimach, T., Krempner, L. A.,
912 Thines, E., Walter, D., Weber, J., Weber, B., Fuchs, B. M., Pöschl, U., and Pöhlker, C.:
913 Bioaerosols in the Amazon rain forest: temporal variations and vertical profiles of
914 Eukarya, Bacteria, and Archaea, *Biogeosciences*, 18, 4873-4887, 10.5194/bg-18-4873-
915 2021, 2021.
- 916 Prospero, J. M., Glaccum, R. A., and Nees, R. T.: Atmospheric transport of soil dust from
917 Africa to South America, *Nature*, 289, 570-572, 10.1038/289570a0, 1981.
- 918 Prospero, J. M., Collard, F.-X., Molinié, J., and Jeannot, A.: Characterizing the annual cycle
919 of African dust transport to the Caribbean Basin and South America and its impact on the
920 environment and air quality, *Global Biogeochem. Cy.*, 28, 757-773,
921 <https://doi.org/10.1002/2013GB004802>, 2014.
- 922 Prospero, J. M., Barkley, A. E., Gaston, C. J., Gatineau, A., Campos y Sansano, A., and
923 Panechou, K.: Characterizing and Quantifying African Dust Transport and Deposition to
924 South America: Implications for the Phosphorus Budget in the Amazon Basin, *Global
925 Biogeochem. Cy.*, 34, e2020GB006536, <https://doi.org/10.1029/2020GB006536>, 2020.
- 926 Ridley, D. A., Heald, C. L., and Ford, B.: North African dust export and deposition: A satellite
927 and model perspective, *J. Geophys. Res.*, 117, <https://doi.org/10.1029/2011JD016794>,
928 2012.
- 929 Ridley, D. A., Heald, C. L., and Prospero, J. M.: What controls the recent changes in African
930 mineral dust aerosol across the Atlantic?, *Atmos. Chem. Phys.*, 14, 5735-5747,
931 10.5194/acp-14-5735-2014, 2014.
- 932 Rizzolo, J. A., Barbosa, C. G. G., Borillo, G. C., Godoi, A. F. L., Souza, R. A. F., Andreoli, R.
933 V., Manzi, A. O., Sá, M. O., Alves, E. G., Pöhlker, C., Angelis, I. H., Ditas, F., Saturno,
934 J., Moran-Zuloaga, D., Rizzo, L. V., Rosário, N. E., Pauliquevis, T., Santos, R. M. N.,
935 Yamamoto, C. I., Andreae, M. O., Artaxo, P., Taylor, P. E., and Godoi, R. H. M.: Soluble
936 iron nutrients in Saharan dust over the central Amazon rainforest, *Atmos. Chem. Phys.*,
937 17, 2673-2687, 10.5194/acp-17-2673-2017, 2017.
- 938 Roberts, A. and Knippertz, P.: Haboobs: Convectively generated dust storms in West Africa,
939 *Weather*, 67, 311 - 316, 2012.
- 940 Ryder, C. L., Highwood, E. J., Lai, T. M., Sodemann, H., and Marsham, J. H.: Impact of
941 atmospheric transport on the evolution of microphysical and optical properties of
942 Saharan dust, *Geophys. Res. Lett.*, 40, 2433-2438, 10.1002/grl.50482, 2013a.
- 943 Ryder, C. L., Highwood, E. J., Rosenberg, P. D., Trembath, J., Brooke, J. K., Bart, M., Dean,
944 A., Crosier, J., Dorsey, J., Brindley, H., Banks, J., Marsham, J. H., McQuaid, J. B.,



- 945 Sodemann, H., and Washington, R.: Optical properties of Saharan dust aerosol and
946 contribution from the coarse mode as measured during the Fennec 2011 aircraft
947 campaign, *Atmos. Chem. Phys.*, 13, 303-325, 10.5194/acp-13-303-2013, 2013b.
- 948 Ryder, C. L., Marengo, F., Brooke, J. K., Estelles, V., Cotton, R., Formenti, P., McQuaid, J. B.,
949 Price, H. C., Liu, D., Ausset, P., Rosenberg, P. D., Taylor, J. W., Choularton, T., Bower,
950 K., Coe, H., Gallagher, M., Crosier, J., Lloyd, G., Highwood, E. J., and Murray, B. J.:
951 Coarse-mode mineral dust size distributions, composition and optical properties from
952 AER-D aircraft measurements over the tropical eastern Atlantic, *Atmos. Chem. Phys.*,
953 18, 17225-17257, 10.5194/acp-18-17225-2018, 2018.
- 954 Salati, E. and Vose, P. B.: Amazon Basin: A System in Equilibrium, *Science*, 225, 129-138,
955 doi:10.1126/science.225.4658.129, 1984.
- 956 Shao, Y., Fink, A. H., and Klose, M.: Numerical simulation of a continental-scale Saharan
957 dust event, *J. Geophys. Res.*, 115, <https://doi.org/10.1029/2009JD012678>, 2010.
- 958 Shao, Y., Klose, M., and Wyrwoll, K.-H.: Recent global dust trend and connections to climate
959 forcing, *J. Geophys. Res.*, 118, 11,107-111,118, <https://doi.org/10.1002/jgrd.50836>,
960 2013.
- 961 Sinyuk, A., Torres, O., and Dubovik, O.: Combined use of satellite and surface observations
962 to infer the imaginary part of refractive index of Saharan dust, *Geophys. Res. Lett.*, 30,
963 <https://doi.org/10.1029/2002GL016189>, 2003.
- 964 SWAP, R., GARSTANG, M., GRECO, S., TALBOT, R., and KÄLLBERG, P.: Saharan dust
965 in the Amazon Basin, *Tellus B*, 44, 133-149, <https://doi.org/10.1034/j.1600-0889.1992.t01-1-00005.x>, 1992.
- 967 Talbot, R. W., Andreae, M. O., Berresheim, H., Artaxo, P., Garstang, M., Harriss, R. C.,
968 Beecher, K. M., and Li, S. M.: Aerosol chemistry during the wet season in central
969 Amazonia: The influence of long-range transport, *J. Geophys. Res.*, 95, 16955-16969,
970 <https://doi.org/10.1029/JD095iD10p16955>, 1990.
- 971 van der Does, M., Korte, L. F., Munday, C. I., Brummer, G. J. A., and Stuut, J. B. W.: Particle
972 size traces modern Saharan dust transport and deposition across the equatorial North
973 Atlantic, *Atmos. Chem. Phys.*, 16, 13697-13710, 10.5194/acp-16-13697-2016, 2016.
- 974 Vitousek, P. M. and Sanford, R. L.: Nutrient Cycling in Moist Tropical Forest, *Annual Review*
975 *of Ecology and Systematics*, 17, 137-167, <http://www.jstor.org/stable/2096992>.1986.
- 976 Wang, J., Christopher, S. A., Brechtel, F., Kim, J., Schmid, B., Redemann, J., Russell, P. B.,
977 Quinn, P., and Holben, B. N.: Geostationary satellite retrievals of aerosol optical
978 thickness during ACE-Asia, *J. Geophys. Res.*, 108,
979 <https://doi.org/10.1029/2003JD003580>, 2003a.
- 980 Wang, J., Christopher, S. A., Reid, J. S., Maring, H., Savoie, D., Holben, B. N., Livingston, J.
981 M., Russell, P. B., and Yang, S.-K.: GOES 8 retrieval of dust aerosol optical thickness
982 over the Atlantic Ocean during PRIDE, *J. Geophys. Res.*, 108,
983 <https://doi.org/10.1029/2002JD002494>, 2003b.
- 984 Wang, Q., Gu, J., and Wang, X.: The impact of Sahara dust on air quality and public health in
985 European countries, *Atmospheric Environment*, 241, 117771,
986 <https://doi.org/10.1016/j.atmosenv.2020.117771>, 2020.
- 987 Wang, Q., Jacob, D. J., Fisher, J. A., Mao, J., Leibensperger, E. M., Carouge, C. C., Le Sager,
988 P., Kondo, Y., Jimenez, J. L., Cubison, M. J., and Doherty, S. J.: Sources of carbonaceous



- 989 aerosols and deposited black carbon in the Arctic in winter-spring: implications for
990 radiative forcing, *Atmos. Chem. Phys.*, 11, 12453-12473, 10.5194/acp-11-12453-2011,
991 2011.
- 992 Wang, Q., Saturno, J., Chi, X., Walter, D., Lavric, J. V., Moran-Zuloaga, D., Ditas, F., Pöhlker,
993 C., Brito, J., Carbone, S., Artaxo, P., and Andreae, M. O.: Modeling investigation of
994 light-absorbing aerosols in the Amazon Basin during the wet season, *Atmos. Chem.*
995 *Phys.*, 16, 14775-14794, 10.5194/acp-16-14775-2016, 2016.
- 996 Wang, W., Evan, A. T., Lavaysse, C., and Flamant, C.: The role the Saharan Heat Low plays
997 in dust emission and transport during summertime in North Africa, *Aeolian Res.*, 28, 1-
998 12, <https://doi.org/10.1016/j.aeolia.2017.07.001>, 2017.
- 999 Wang, Y., Jacob, D. J., and Logan, J. A.: Global simulation of tropospheric O₃-NO_x -
1000 hydrocarbon chemistry: 1. Model formulation, *J. Geophys. Res.*, 103, 10713-10725,
1001 <https://doi.org/10.1029/98JD00158>, 1998.
- 1002 Wesely, M. L.: Parameterization of surface resistances to gaseous dry deposition in regional-
1003 scale numerical models, *Atmos. Environ.*, 41, 52-63,
1004 <https://doi.org/10.1016/j.atmosenv.2007.10.058>, 2007.
- 1005 Wu, L., Li, X., Kim, H., Geng, H., Godoi, R. H. M., Barbosa, C. G. G., Godoi, A. F. L.,
1006 Yamamoto, C. I., de Souza, R. A. F., Pöhlker, C., Andreae, M. O., and Ro, C. U.: Single-
1007 particle characterization of aerosols collected at a remote site in the Amazonian
1008 rainforest and an urban site in Manaus, Brazil, *Atmos. Chem. Phys.*, 19, 1221-1240,
1009 10.5194/acp-19-1221-2019, 2019.
- 1010 Ysard, N., Jones, A. P., Demyk, K., Boutéraon, T., and Koehler, M.: The optical properties of
1011 dust: the effects of composition, size, and structure, *A&A*, 617, A124, 2018.
- 1012 Yu, H., Chin, M., Bian, H., Yuan, T., Prospero, J. M., Omar, A. H., Remer, L. A., Winker, D.
1013 M., Yang, Y., Zhang, Y., and Zhang, Z.: Quantification of trans-Atlantic dust transport
1014 from seven-year (2007–2013) record of CALIPSO lidar measurements, *Remote Sens.*
1015 *Environ.*, 159, 232-249, <https://doi.org/10.1016/j.rse.2014.12.010>, 2015a.
- 1016 Yu, H., Chin, M., Yuan, T., Bian, H., Remer, L. A., Prospero, J. M., Omar, A., Winker, D.,
1017 Yang, Y., Zhang, Y., Zhang, Z., and Zhao, C.: The fertilizing role of African dust in the
1018 Amazon rainforest: A first multiyear assessment based on data from Cloud-Aerosol Lidar
1019 and Infrared Pathfinder Satellite Observations, *Geophys. Res. Lett.*, 42, 1984-1991,
1020 10.1002/2015GL063040, 2015b.
- 1021 Yu, Y., Kalashnikova, O. V., Garay, M. J., Lee, H., Notaro, M., Campbell, J. R., Marquis, J.,
1022 Ginoux, P., and Okin, G. S.: Disproving the Bodélé Depression as the Primary Source of
1023 Dust Fertilizing the Amazon Rainforest, *Geophysical Research Letters*, 47, 2020.
- 1024 Yu, H., Tan, Q., Chin, M., Remer, L. A., Kahn, R. A., Bian, H., Kim, D., Zhang, Z., Yuan, T.,
1025 Omar, A. H., Winker, D. M., Levy, R. C., Kalashnikova, O., Crepeau, L., Capelle, V., and
1026 Chédin, A.: Estimates of African Dust Deposition Along the Trans-Atlantic Transit Using
1027 the Decadelong Record of Aerosol Measurements from CALIOP, MODIS, MISR, and
1028 IASI, *J. Geophys. Res.*, 124, 7975-7996, <https://doi.org/10.1029/2019JD030574>, 2019.
- 1029 Yuan, T., Yu, H., Chin, M., Remer, L. A., McGee, D., and Evan, A.: Anthropogenic Decline of
1030 African Dust: Insights From the Holocene Records and Beyond, *Geophys. Res. Lett.*, 47,
1031 e2020GL089711, <https://doi.org/10.1029/2020GL089711>, 2020.
- 1032 Zender, C. S., Bian, H., and Newman, D.: Mineral Dust Entrainment and Deposition (DEAD)



1033 model: Description and 1990s dust climatology, *J. Geophys. Res.*, 108,
1034 <https://doi.org/10.1029/2002JD002775>, 2003.
1035 Zhang, L., Gong, S., Padro, J., and Barrie, L.: A size-segregated particle dry deposition
1036 scheme for an atmospheric aerosol module, *Atmos. Environ.*, 35, 549-560,
1037 [https://doi.org/10.1016/S1352-2310\(00\)00326-5](https://doi.org/10.1016/S1352-2310(00)00326-5), 2001.
1038 Zhang, L., Kok, J. F., Henze, D. K., Li, Q., and Zhao, C.: Improving simulations of fine dust
1039 surface concentrations over the western United States by optimizing the particle size
1040 distribution, *Geophys. Res. Lett.*, 40, 3270-3275, [10.1002/grl.50591](https://doi.org/10.1002/grl.50591), 2013.
1041
1042
1043
1044
1045



1046 **Table 1.** Annual and seasonal dust emissions (Pg a^{-1}) in northern Africa ($17.5^\circ \text{W} -$
 1047 $40^\circ \text{E}, 10^\circ \text{N} - 35^\circ \text{N}$)^a.

Year	Spring	Summer	Fall	Winter	Annual (Wet season)
2013	1.2	0.77	0.48	1.0	0.88 (1.1)
2014	0.83	0.84	0.51	0.91	0.77 (0.89)
2015	1.2	0.46	0.33	1.1	0.77 (1.3)
2016	0.82	0.52	0.37	0.89	0.65 (0.86)
2017	0.68	0.38	0.47	0.70	0.56 (0.63)
Mean \pm std ^b	0.95 \pm 0.24	0.59 \pm 0.20	0.43 \pm 0.078	0.92 \pm 0.15	0.73 \pm 0.12 (0.96 \pm 0.25)

1048 ^a Spring: March – May; Summer: June – August; Fall: September – November; Winter: January,
 1049 February, and December; Wet season: January – April

1050 ^b standard deviation

1051

1052

1053 **Table 2.** Mass fractions (%) of dust emitted in each bin for different particle mass size
 1054 distribution (PMSD) schemes tested in GEOS-Chem.

Scheme	bin 1				bin 2	bin 3	bin 4
	sub-bin 1	sub-bin 2	sub-bin 3	sub-bin 4			
	(0.1 – 0.18) ^a (3.1) ^b	(0.18 – 0.3) ^a (4.3) ^b	(0.3 – 0.6) ^a (2.7) ^b	(0.6 – 1.0) ^a (0.96) ^b			
V12	0.7	3.32	24.87	71.11	19.2	34.9	38.2
V12_C	6	12	24	58.00	25.3	32.2	30.2
V12_F	3.9	8.06	43	45.04	11.9	15.6	67

1055 ^a size range in radius (μm) for each bin

1056 ^b mass extinction efficiency (MEE) at wavelength of 550 nm in unit of $\text{m}^2 \text{g}^{-1}$ for dust particles in
 1057 each bin in the GEOS-Chem model

1058

1059

1060

1061

1062

1063



1064

1065 **Table 3.** Estimates of annual dust and associated phosphorus deposition into the

1066

Amazon Basin.

Methods	Dust deposition		P deposition		References
	total (Tg a ⁻¹)	flux (g m ⁻² a ⁻¹)	total (Tg a ⁻¹)	flux (mg m ⁻² a ⁻¹)	
CESM2	10 ± 2.1	n/a	0.0077±0.0016	n/a	Li et al. (2021) ^a
AeroCom Phase I	7.7	0.81	0.0063	0.66	Kok et al. (2021) ^b
MERRA-2	8.0	1.05	0.0062	0.9	Prospero et al. (2020) ^a
MERRA-2, CAM	n/a	n/a	0.011 – 0.033	1.1 – 3.5	Barkley et al. (2019) ^a
GLOMAP	32	1.8	0.019	1.1	Herbert et al. (2018) ^a
CALIOP	8– 48	0.8 – 5	0.006 – 0.037	0.7 – 3.9	Yu et al. (2015b) ^a
ECHAM5	30.3/11.4	n/a	0.025/0.0093	n/a	Gläser et al. (2015) ^b
GEOS-Chem	17± 5	n/a	0.014	n/a	Ridley et al. (2012) ^b
MATCH	n/a	n/a	n/a	0.48	Mahowald et al. (2005) ^a
MODIS	50	n/a	0.041	n/a	Kaufman (2005) ^b
Field measurement	13	19	0.011	16	Swap et al. (1992) ^b
GEOS-Chem	10 ± 1.7	1.2 ± 0.20	0.0085 ± 0.0014	0.97 ± 0.16	This study

1067 *Note.* Table extracted in part from Prospero et al. (2020).

1068 ^a The P mass fraction is 0.077% for Li et al. (2021) and Prospero et al. (2020), 0.108% for Barkley
 1069 et al. (2019), 0.088% for Herbert et al. (2018), 0.078% for Yu et al. (2015b), and 0.07% for
 1070 Mahowald et al. (2005).

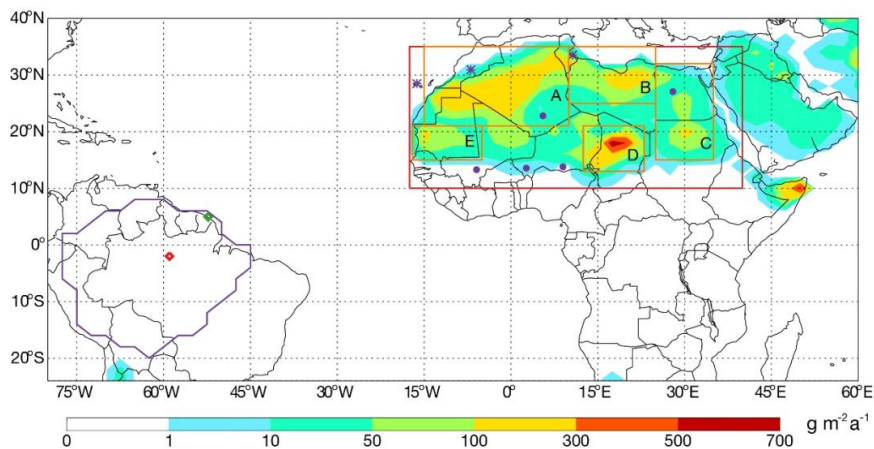
1071 ^b Assuming P mass fraction of 0.082% in dust, the same value as used in this study.

1072

1073

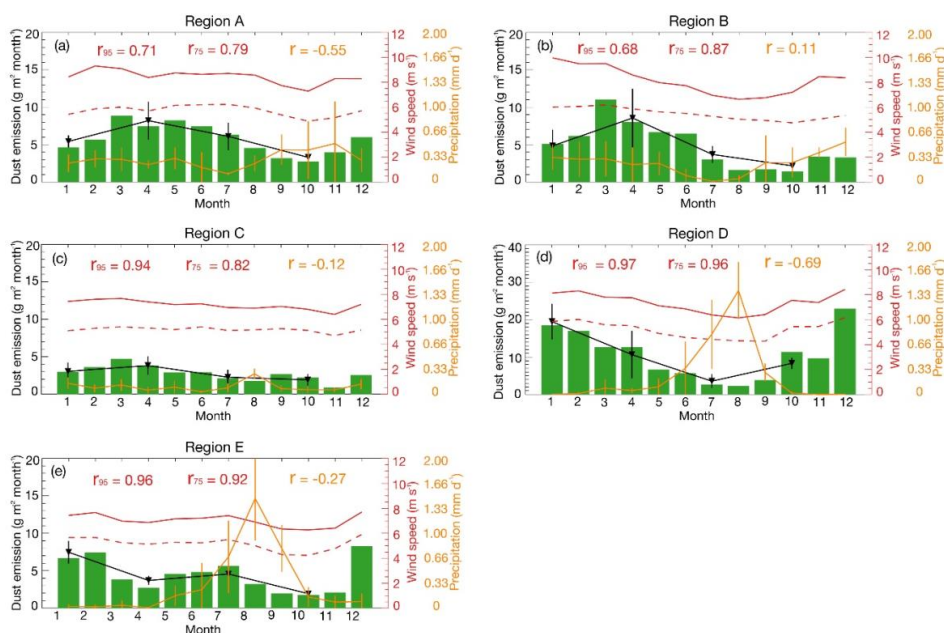
1074

1075



1076

1077 **Figure 1.** Simulated dust emissions in GEOS-Chem, averaged from 2013 to 2017. The
1078 location of AERONET sites used in Figure 3 are marked as purple symbols, of which
1079 circles represent the sites used in Figure 4. The region of the Amazon Basin is defined
1080 by purple lines. The location of Cayenne site in the northeast coast of South America
1081 and ATTO site in the central Amazon Basin are marked as green and red diamonds,
1082 respectively. The red rectangle illustrates the area of northern Africa (17.5° W – 40° E,
1083 10° N – 35° N) and the orange rectangles shows the areas of five major source regions
1084 described in the text (A: 15° W – 10° E, 21° N – 35° N; B: 10° E – 25° E, 25° N – 35°
1085 N; C: 25° E – 35° E, 15° N – 32° N; D: 12.5° E – 23° E, 13° N – 21° N; E: 17° W – 5°
1086 W, 15° N – 21° N).
1087

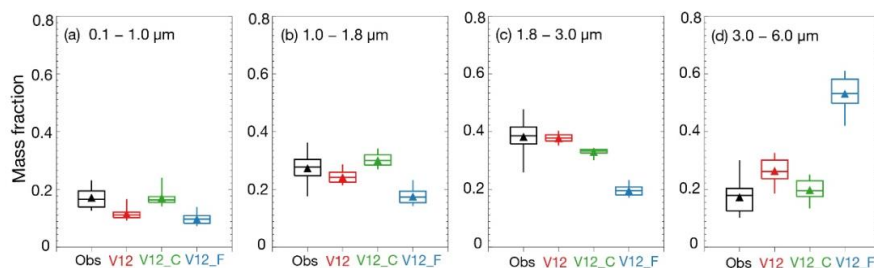


1088

1089 **Figure 2.** Monthly dust emission fluxes together with the 95th percentile hourly wind
 1090 speeds (red solid lines), the 75th percentile hourly wind speeds (red dotted lines) and
 1091 precipitation (yellow lines) over the five major source regions averaged from 2013 to
 1092 2017. Seasonal emission fluxes of dust are also shown as black lines. The correlation
 1093 coefficients (r) between the dust emission fluxes and different meteorological variables
 1094 are also shown in each panel.

1095

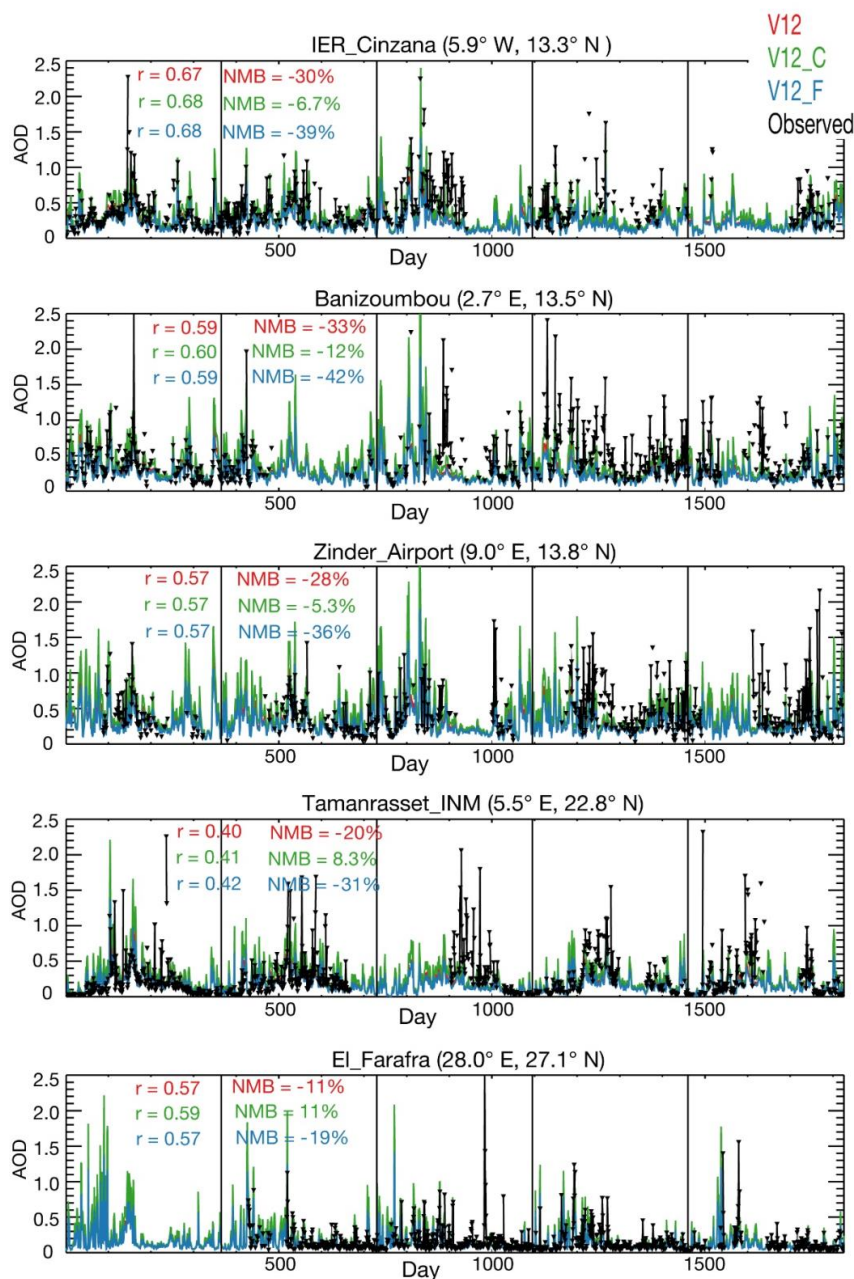
1096



1097

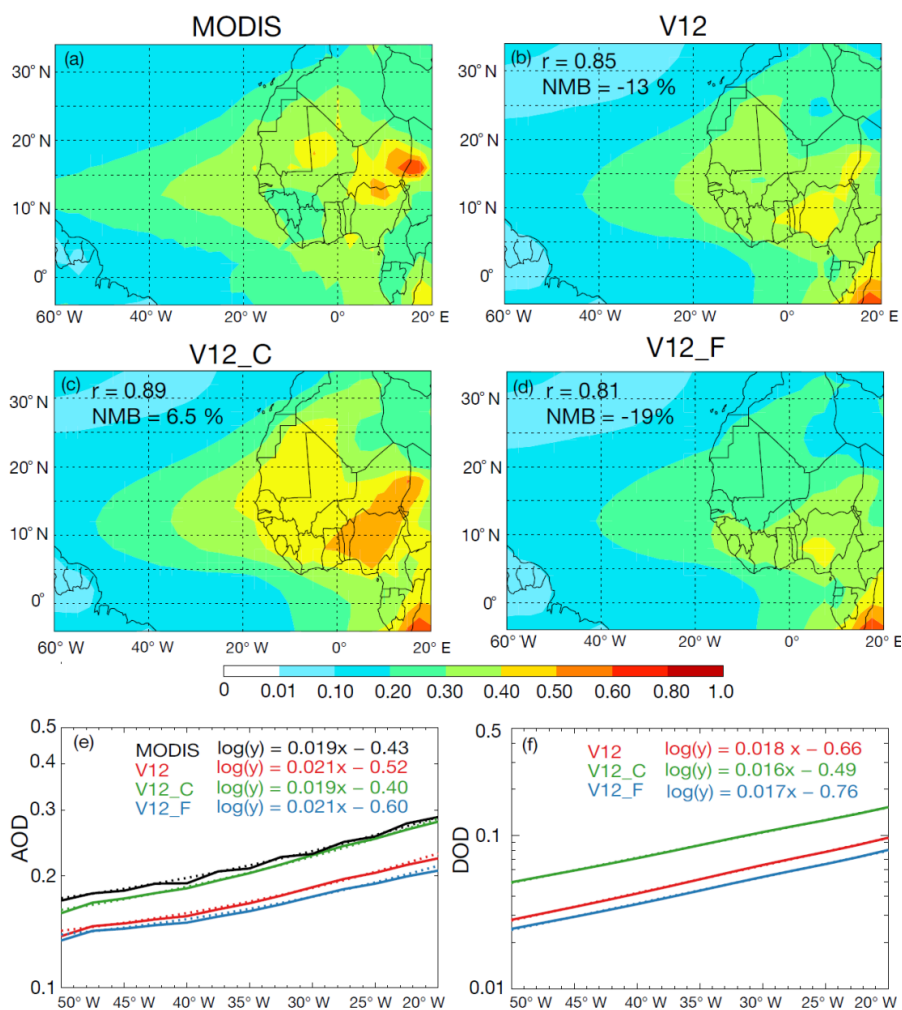
1098 **Figure 3.** Boxplots of the mass fractions of column-integrated aerosols in the four size
 1099 bins (in radius) retrieved from AERONET sites over Africa compared with model
 1100 results based on different PMSD schemes. The triangles represent the mean values.

1101



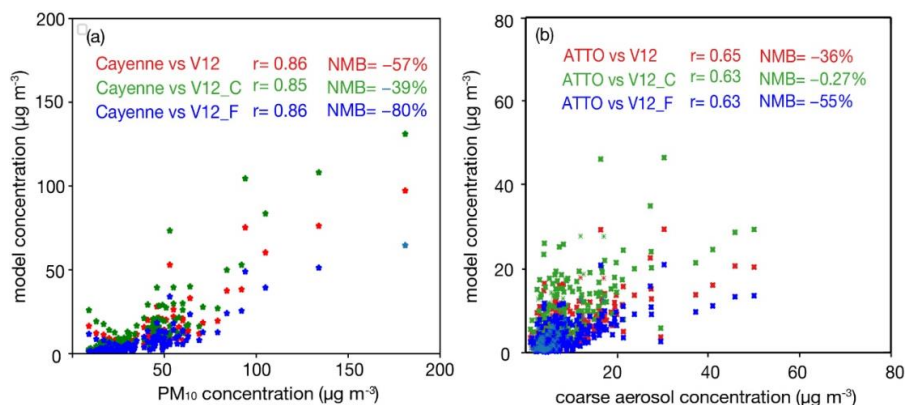
1102
1103
1104
1105
1106

Figure 4. Time series of AERONET (black lines) and simulated daily AOD (at wavelength of 675 nm) during 2013 – 2017. Normalized mean bias (NMB) and correlation (r) statistics between the AERONET and simulated data are shown as inset.



1107

1108 **Figure 5.** (a) – (d) Spatial distributions of observed and simulated AOD (at 550 nm)
 1109 over the region of 60° W – 20° E and 10° N – 35° N averaged over 2013 – 2017.
 1110 Normalized mean bias (NMB) and correlation coefficient (r) between the simulations
 1111 and MODIS AOD are shown as inset. (e) MODIS (black) and simulated (color) AOD
 1112 and (f) simulated dust optical depth (DOD) at 550 nm along the transect from 20° to
 1113 50° W, averaged over 5° S – 25° N for the period 2013 – 2017. The solid lines represent
 1114 averaged data and the dashed lines are the logarithmic trend lines.
 1115

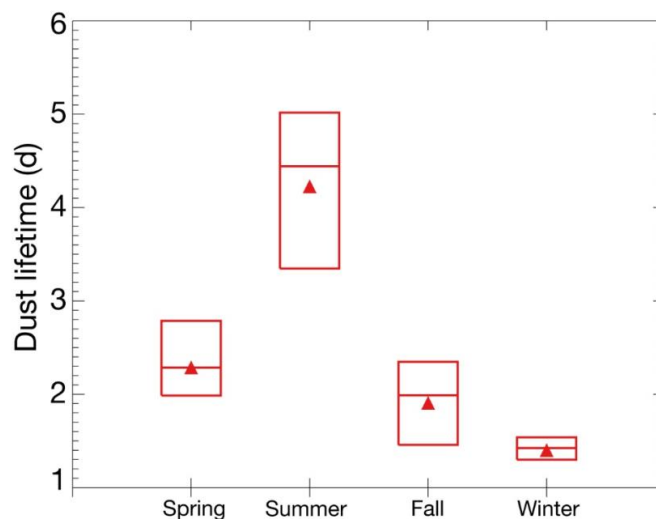


1116

1117 **Figure 6.** Scatter plots of (a) observed PM_{10} and simulated dust concentrations at
1118 Cayenne site during wet season of 2014 and (b) observed coarse aerosol (PM_{1-10}) and
1119 simulated dust concentrations at ATTO site during wet season of 2014-2016.
1120 Normalized mean bias (NMB) and correlation (r) statistics between the observation and
1121 simulation are shown as inset.

1122

1123

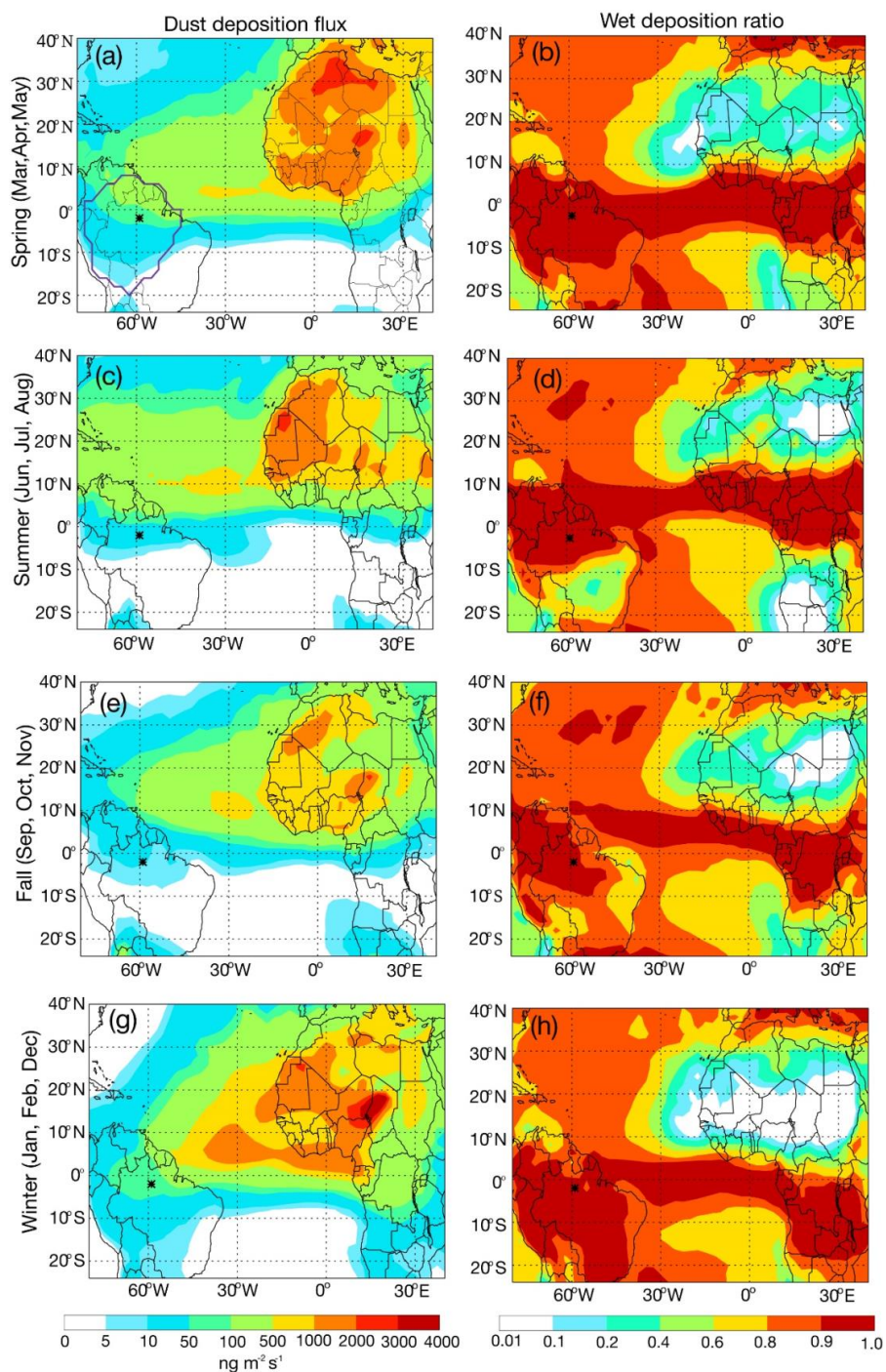


1124

1125 **Figure 7.** Seasonal e-folding lifetime derived from the logarithm of simulated dust
1126 column burden against travel time along the transect from 20° W to 50° W averaged
1127 over 5° S – 25° N during the period of 2013 – 2017. The triangles represent the mean
1128 values, and the bottom and top sides of the boxes represent the minimums and
1129 maximums.



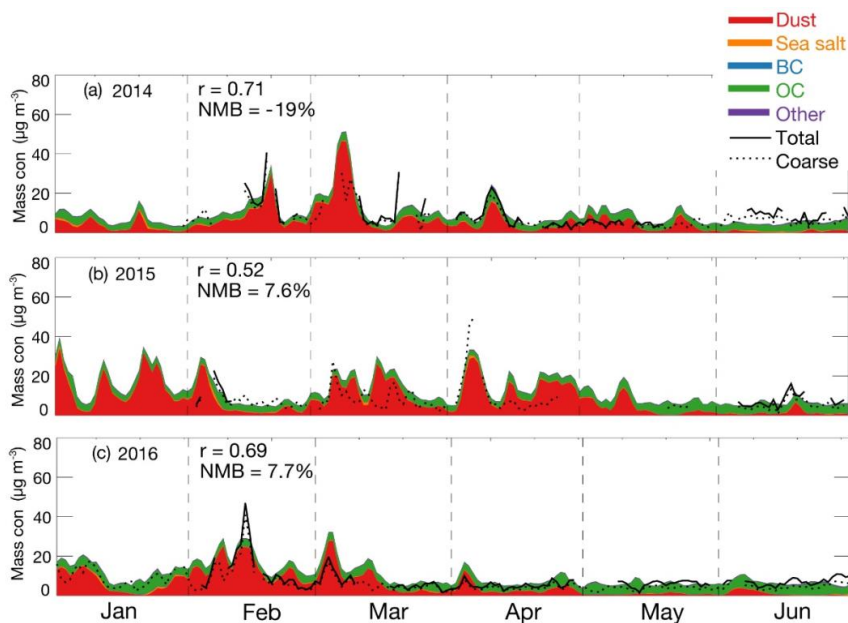
1130



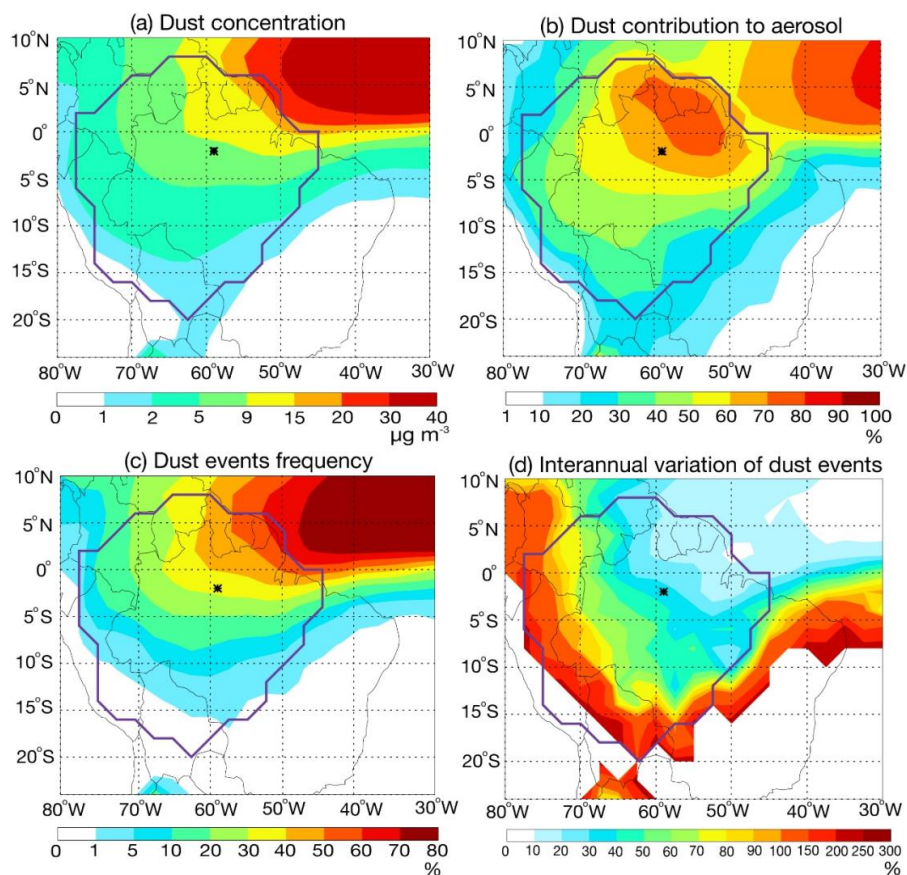
1131



1132 **Figure 8.** Simulated seasonal (left) dust deposition fluxes and (right) contribution of
1133 wet deposition during 2013-2017. The ATTO site is marked as asterisk. The region of
1134 the Amazon Basin is defined by purple lines in Figure 7a.

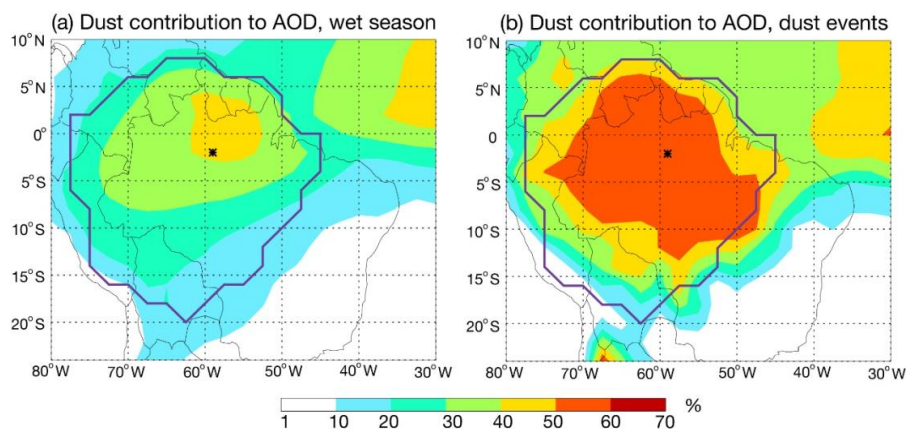


1135
1136 **Figure 9.** Time series of observed coarse and total aerosol mass concentrations and
1137 simulated aerosol species concentrations at the ATTO site from January to June in (a)
1138 2014, (b) 2015, and (c) 2016. Model results are separated into different species shown
1139 as stacked areas. Normalized mean bias (NMB) and correlation coefficient (r) between
1140 the observed coarse aerosols and simulated dust concentrations are shown as inset.
1141



1142
1143 **Figure 10.** (a) simulated surface dust concentration and (b) its contribution to surface
1144 aerosol concentration over the Amazon Basin in the wet season of 2013-2017. (c) the
1145 frequency of dust events and (d) its interannual variation (namely relative standard
1146 deviation) during the same period. The location of ATTO site is marked as asterisks.
1147 The region of Amazon Basin is marked by purple lines.

1148
1149



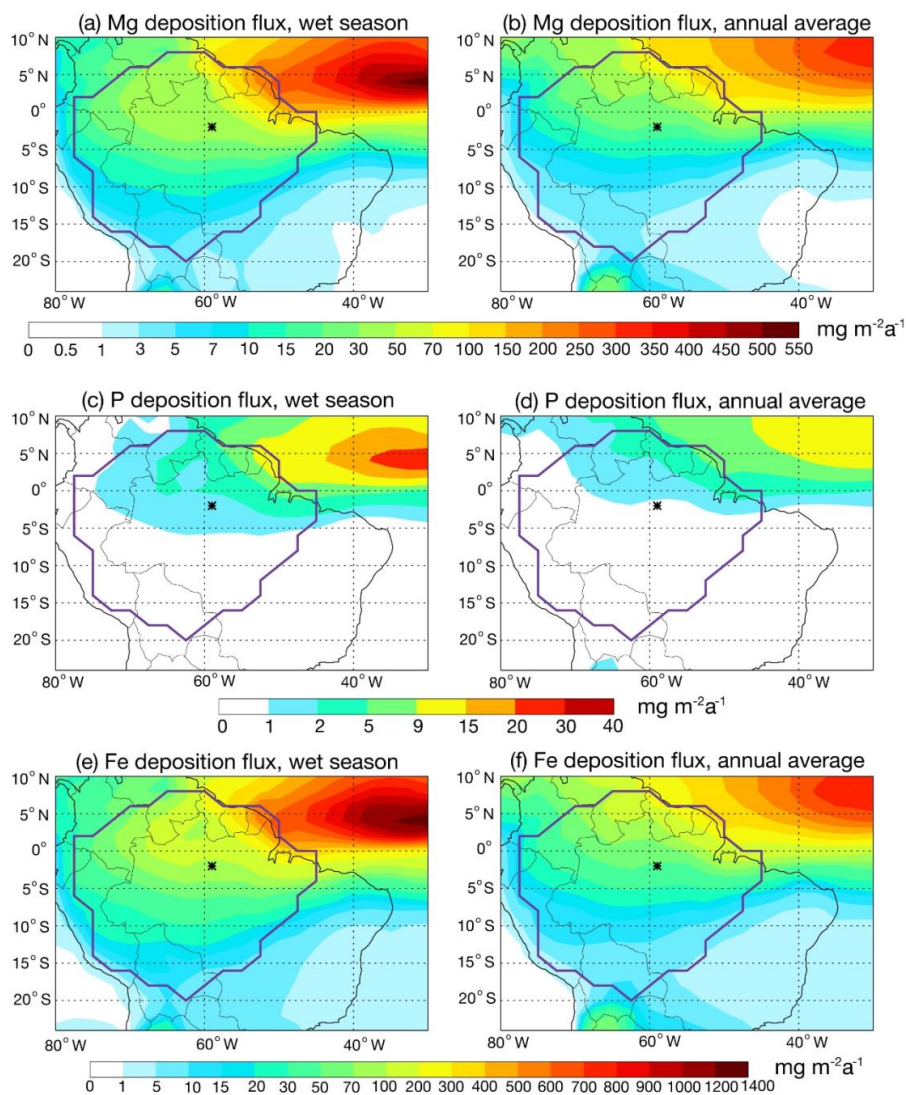
1150

1151 **Figure 11.** Dust contribution to total AOD at 675 nm over the Amazon Basin averaged
1152 over the (a) wet season and (b) dust events during 2013-2017. The region of Amazon
1153 Basin is marked by purple lines.

1154

1155

1156



1157

1158 **Figure 12.** Magnesium deposition flux in (a) wet season and (b) annual averaged from
1159 2013 to 2017. Phosphorus deposition flux in (c) wet season and (d) annual averaged
1160 from 2013 to 2017. Iron deposition flux in (e) wet season and (f) annual averaged from
1161 2013 to 2017. The location of ATTO site is marked as asterisks. The region of Amazon
1162 Basin is marked by purple lines.

1163

1164